J. Fluid Mech. (2013), *vol.* 730, *pp.* 559–592.
doi:10.1017/jfm.2013.346

Wavepackets in the velocity field of turbulent jets

André V. G. Cavalieri[1,2,†], Daniel Rodríguez[3,4], Peter Jordan[1], Tim Colonius[3] and Yves Gervais[1]

[1]Département Fluides, Thermique, Combustion, Institut PPrime, CNRS–Université de Poitiers–ENSMA, Poitiers, France

[2]Divisão de Engenharia Aeronáutica, Instituto Tecnológico de Aeronáutica, São José dos Campos, SP, Brazil

[3]Division of Engineering and Applied Science, California Institute of Technology, Pasadena, CA 91125, USA

[4]School of Aeronautics, Universidad Politécnica de Madrid, Madrid, Spain

(Received 30 November 2012; revised 10 May 2013; accepted 1 July 2013; first published online 2 August 2013)

We study the velocity fields of unforced, high Reynolds number, subsonic jets, issuing from round nozzles with turbulent boundary layers. The objective of the study is to educe wavepackets in such flows and to explore their relationship with the radiated sound. The velocity field is measured using a hot-wire anemometer and a stereoscopic, time-resolved PIV system. The field can be decomposed into frequency and azimuthal Fourier modes. The low-angle sound radiation is measured synchronously with a microphone ring array. Consistent with previous observations, the azimuthal wavenumber spectra of the velocity and acoustic pressure fields are distinct. The velocity spectrum of the initial mixing layer exhibits a peak at azimuthal wavenumbers m ranging from 4 to 11, and the peak is found to scale with the local momentum thickness of the mixing layer. The acoustic pressure field is, on the other hand, predominantly axisymmetric, suggesting an increased relative acoustic efficiency of the axisymmetric mode of the velocity field, a characteristic that can be shown theoretically to be caused by the radial compactness of the sound source. This is confirmed by significant correlations, as high as 10 %, between the axisymmetric modes of the velocity and acoustic pressure fields, these values being significantly higher than those reported for two-point flow–acoustic correlations in subsonic jets. The axisymmetric and first helical modes of the velocity field are then compared with solutions of linear parabolized stability equations (PSE) to ascertain if these modes correspond to linear wavepackets. For all but the lowest frequencies close agreement is obtained for the spatial amplification, up to the end of the potential core. The radial shapes of the linear PSE solutions also agree with the experimental results over the same region. The results suggests that, despite the broadband character of the turbulence, the evolution of Strouhal numbers $0.3 \leqslant St \leqslant 0.9$ and azimuthal modes 0 and 1 can be modelled as linear wavepackets, and these are associated with the sound radiated to low polar angles.

Key words: absolute/convective instability, hydrodynamic noise, jet noise

† Email address for correspondence: andre@ita.br

1. Introduction

Since the first observations of coherent structures in turbulent jets (Crow & Champagne 1971; Moore 1977), instability waves, or wavepackets, have been postulated as a possible sound source mechanism (Crow & Champagne 1971; Michalke 1971; Crow 1972). Associated sound source models have been explored in subsonic (Mankbadi & Liu 1984) and supersonic (Tam & Burton 1984; Tam & Chen 1994) regimes. Wavepackets comprise hydrodynamic waves with amplitude growth, saturation and decay. Their spatial extension is much greater than turbulence length scales, and, as we will show, their fluctuation energy is considerably less than that of those eddies that dominate the turbulent kinetic energy. Because of their large spatial extension, wavepackets constitute a non-compact sound source, and, on account of their azimuthal coherence, are more acoustically efficient than the more energetic, but compact, stochastic eddies thought to dominate sound radiation at the time of Lighthill (1952). A recent review of wavepackets and turbulent jet noise has been provided by Jordan & Colonius (2013).

Many early studies seeking to compare wavepackets in turbulent jets with stability theory involved *forced jets* (Crighton & Gaster 1976; Cohen & Wygnanski 1987; Petersen & Samet 1988), whose phase-locked disturbances are more easily measured experimentally. But the extension of the conclusions of such studies to their unforced counterparts is not straightforward. In natural jets the signature of azimuthally coherent wavepackets is clearest in the near pressure field, whose energy is concentrated in a few low-order azimuthal modes, in contrast to the velocity field (Michalke & Fuchs 1975; Armstrong, Fuchs & Michalke 1977; Fuchs & Michel 1978). Measurements using line arrays of microphones in the near field reveal a hydrodynamic wave extending several jet diameters downstream of the nozzle exit (Picard & Delville 2000; Tinney & Jordan 2008).

The recent results of Suzuki & Colonius (2006) and Gudmundsson & Colonius (2011) show that the pressure field just outside the jet can be modelled quite accurately as a superposition of linear wavepackets with different frequencies and azimuthal modes, but it remains to be established if these models accurately predict the velocity field of these structures within the jet. The hydrodynamic waves have small amplitudes, no fixed phase reference, and their signature is therefore difficult to educe from the velocity field of unforced jets (a recent attempt has been made by Kerhervé *et al.* 2012 using data from a large eddy simulation). The signature is, on the other hand, relatively clear in forced jets (Crow & Champagne 1971; Hussain & Zaman 1981; Cohen & Wygnanski 1987; Petersen & Samet 1988) and transitional flows, i.e. jets with laminar boundary layers at the nozzle exit (Becker & Massaro 1968; Yule 1978; Laufer & Yen 1983; Violato & Scarano 2011). In both cases the velocity field, at least for small distances from the nozzle exit, is dominated by coherent structures, whose amplitude is far greater than those of natural jets with turbulent boundary layers. Nonlinear saturation and vortex dynamics are also clearly evident in these strongly forced flows. This is clearly not the case for natural jets with turbulent boundary layers at the nozzle exit.

Gudmundsson & Colonius (2011) present a comparison between results of linear parabolized stability equations (hereafter PSE) and the velocity field of unforced jets, measured using PIV in cross-sections. In that work the PIV measurements were not time-resolved, and so comparison for individual frequencies was not possible; the wavepackets had to be superposed prior to comparison with experiment. The results showed encouraging agreement, which motivated the present experiment whose goal is frequency-dependent comparisons between wavepacket models and measurements.

We present experimental results that probe the velocity fields of unforced, turbulent jets to determine if the low-order azimuthal modes of the velocity field can be modelled as linear wavepackets. Linear PSE are used, as in the work of Gudmundsson & Colonius (2011), as this allows the evolution of wavepackets on a slowly diverging mean flow to be modelled. Linear PSE are used here as a reference model for hydrodynamic waves resulting from the Kelvin–Helmholtz instability in the initial region of the jet. And while the results constitute a partial validation of linear PSE as an appropriate model, our view is that they provide a more general assessment of the presence of such linear waves in unforced turbulent jets, and of the possibility of using a linear model for turbulent velocity fluctuations if the experimental mean velocity profile is used as the base flow for linearization.

A further motivation for this study is the observation, by Cavalieri *et al.* (2012), that the sound field radiated by the jets we study are consistent with sound radiation by non-compact wavepackets with low azimuthal wavenumber. Most notably, the sound field at low polar angles is predominantly axisymmetric, and *superdirective*, as one would expect from an axially non-compact, wavepacket, sound source. This suggests that an axisymmetric wavepacket within the turbulent field drives the low-angle radiation, and we confirm this by studying the correlation between the azimuthal Fourier modes of the velocity and acoustic fields.

The paper is organized as follows. The experimental setup is described in § 2. In § 3.1 we evaluate the dominant azimuthal wavenumbers in both the velocity and the acoustic fields, and the relationship between the azimuthal modes of turbulence and sound is investigated by means of correlations in § 3.2. A brief description of the computational approach for linear PSE is presented in § 4.1. We perform comprehensive comparisons of this model with the experimental results. We first take advantage of the symmetry properties of circular jets, assessing the axisymmetric mode on the jet centreline, using hot-wire measurements, in § 4.2. To obtain results for the helical modes, and at radial positions other than the centreline, stereoscopic time-resolved PIV measurements are made in cross-stream planes at several axial stations. The comparison of the experimental results with linear PSE are presented in § 4.3, accompanied by a general discussion regarding wavepackets in turbulent jets.

2. Experimental setup

The experiments were performed in the 'Bruit et Vent' anechoic facility at the Centre d'Etudes Aérodynamiques et Thermiques (CEAT), Institut PPrime, Poitiers, France. The anechoic chamber has dimensions of 9.6 m $\times$ 6 m $\times$ 3.4 m, and is covered with absorbing foam of depth equal to 0.4 m. The cut-off frequency of the chamber is 212 Hz. Since frequencies below this value in the acoustic field are contaminated by reflected acoustic waves, all acoustic signals were high-pass filtered using a finite impulse response filter. The flow in the facility follows a closed loop, and is driven by fans located outside the facility. Downstream of the fans, the flow passes through lined ducts designed to absorb the ventilator noise. More details can be found in Kœnig (2011).

We carried out velocity measurements of subsonic jets with acoustic Mach numbers equal to 0.4, 0.5 and 0.6. The nozzle diameter, D, was 0.05 m. With these conditions, the Reynolds number, $\rho UD/\mu$, varies from 4.2×10^5 to 5.7×10^5, where ρ, U and μ are, respectively, the density, axial velocity and the viscosity at the nozzle exit.

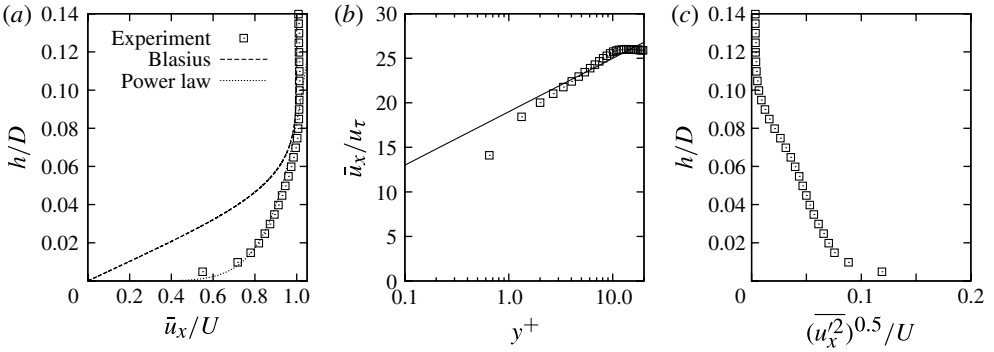

FIGURE 1. Boundary layer profiles at the nozzle exit for the Mach 0.5 jet: (*a*) mean velocity, (*b*) mean velocity in wall units, and (*c*) r.m.s. value. The power law in (*a*) is given by $\bar{u}_x/U = (y/\delta)^{1/7}$, and the straight line in (*b*) has slope of $1/\kappa$, with von Kármán constant κ equal to 0.384.

The velocity field is described in cylindrical coordinates (x, r, ϕ), which are respectively the axial, radial and azimuthal coordinates. Spherical coordinates (R, θ, Φ), respectively radius, polar and azimuthal angle, are used to describe the sound field. The polar angle is measured from the downstream jet axis. Both coordinate systems have their origin at the nozzle exit.

A convergent section was located upstream of the jet exit, with an area contraction of 31. This was followed by a straight circular section of length 150 mm; a boundary layer trip was used to force transition 135 mm upstream (2.7D) of the nozzle exit. To establish whether the boundary layers at the nozzle exit are turbulent, hot-wire results for the boundary layer are shown in figure 1. The velocity profile of turbulent boundary layers presents an overlap region that can be fitted using either a power law or a log law, as discussed by Österlund *et al.* (2000). The use of a power law in y/δ, where δ is the boundary layer thickness, is straightforward, and leads to a close approximation of the velocity profile with $(y/\delta)^{1/7}$ (Schlichting 1979), as shown in figure 1(*a*).

On the other hand, application of the log law requires that distances and velocities be made non-dimensional with wall quantites given by $y^+ = \rho y u_\tau/\mu$ and $u_\tau = \sqrt{\tau/\rho}$, where τ is the shear stress on the wall. We do not have measurements of the shear stress, and the thin boundary layers in our experiment do not allow an accurate determination of the shear stress using the velocity gradient. Hence, we have used the fit of the skin-friction coefficient given by Österlund *et al.* (2000) to estimate u_τ in our experiment. Taking the von Kármán constant κ equal to 0.384, as in Österlund *et al.* (2000), leads to further confirmation that the present boundary layers are turbulent, as shown by the comparison of the measurements with the expected slope of $1/\kappa$ in the overlap region (figure 1*b*).

The thickness δ of the boundary layer, as well as the momentum thickness δ_2, are shown in table 1 for the three Mach numbers. The present jet setup was previously used for acoustic measurements with an azimuthal microphone ring (Cavalieri *et al.* 2012).

Velocity measurements were obtained using a traversing single hot-wire and with stereoscopic, time-resolved particle image velocimetry (TR-PIV). The hot-wire was calibrated *in situ* using the procedure described by Tutkun *et al.* (2009), with a

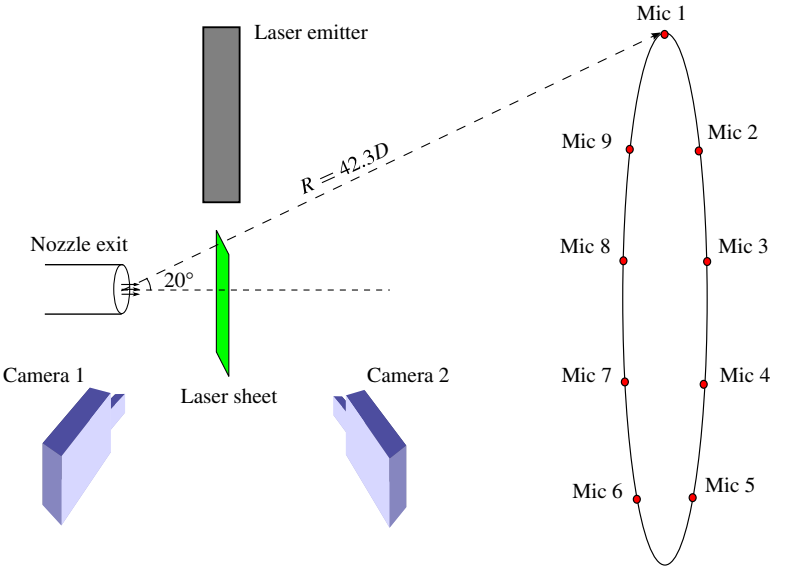

FIGURE 2. (Colour online) Scheme of the experimental setup for time-resolved PIV and acoustic measurements.

M	δ (mm)	δ/D	δ_2 (mm)	δ_2/D	Re	Re_δ	$Re_{\delta 2}$
0.4	4.5	9.0×10^{-2}	0.477	9.5×10^{-3}	4.2×10^5	3.8×10^4	4.0×10^3
0.5	4.25	8.5×10^{-2}	0.401	8.0×10^{-3}	5.0×10^5	4.3×10^4	4.0×10^3
0.6	4.25	8.5×10^{-2}	0.396	7.9×10^{-3}	5.7×10^5	4.9×10^4	4.5×10^3

TABLE 1. Boundary layer thickness δ, momentum thickness δ_2 at the nozzle exit, and Reynolds numbers of each jet flow.

traversing Pitot tube giving the mean axial velocity. Wires with diameter of 2.5 μm and length of 0.7 mm, which is about 0.15δ, were used with a Dantec 55M01 anemometer; the corner frequency of this setup was 30 kHz, corresponding to Strouhal numbers between 7 and 11, depending on the jet velocity. This Strouhal number is sufficiently high to avoid significant aliasing effects in the low-frequency energy-containing part of the hot-wire spectra. Calculation of power spectra was performed by averaging 400 blocks of data without overlap, with frequency resolution corresponding to $\Delta St = 0.022$ for the $M = 0.4$ jet.

The stereoscopic TR-PIV experiments were performed with a setup shown schematically in figure 2. The measurements are performed in cross-stream planes, as in Tinney, Glauser & Ukeiley (2008) and Kœnig *et al.* (2011*b*). Two cameras were placed at an angle of 45° to the laser plane, one placed upstream and the other downstream of the plane, positioned so as to sense forward light scattering by the particles. The flow was seeded with glycerin-based smoke. Particle sizes ranged from 0.5 to 1 μm. For the frequencies considered in this study (Nyquist frequency of 2.5 kHz), the analysis in Tinney *et al.* (2008) shows that the particle tracing errors are negligible for a particle size of 1 μm or lower. A schematic drawing of the experimental setup is shown in figure 2, and the mean axial velocities for the $M = 0.4$

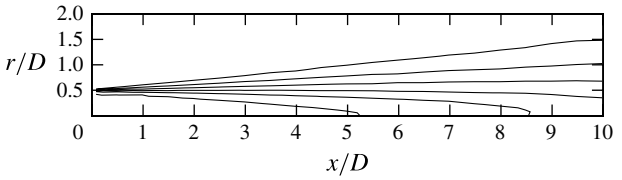

FIGURE 3. Mean axial velocity for the $M = 0.4$ jet. Contours are equally spaced from $0.1U$ to $0.99U$.

jet are shown in figure 3; the differences in the mean flows for $M = 0.5$ and $M = 0.6$ are slight. For all jets the end of the potential core is between 5 and $5.5D$.

The sampling frequency was 5 kHz, which corresponds to $St = 1.82$, 1.46 and 1.21 for the $M = 0.4$, 0.5 and 0.6 jets, respectively. A total of 19 414 image pairs were recorded. Image-processing consisted of a five-pass correlation routine with 64×64 pixel correlation for the first pass, 16×16 pixel for the final pass and with a 50 % correlation overlap at each pass, done with LaVision software DaVis 8; this leads to velocity fields with 114×102 velocity vectors. This grid was subsequently interpolated to cylindrical coordinates to allow the expansion of the velocity field in azimuthal Fourier modes. Frequency spectra were calculated using averages of blocks with 50 % overlap. The number of samples in each block was chosen so as to provide a resolution in Strouhal number of $\Delta St = 0.025$. All power spectral densities presented in this work are single-sided.

We simultaneously measured the acoustic pressure with an azimuthal ring of nine microphones at a polar angle $\theta = 20°$, with a distance R to the nozzle exit equal to $42.3D$, as illustrated in figure 2. These measurements allowed calculation of flow–acoustic correlations in two ways: the first was between a single point in the velocity field and a single microphone, as often done in the literature (Lee & Ribner 1972; Schaffar 1979; Juvé, Sunyach & Comte-Bellot 1980; Panda, Seasholtz & Elam 2005; Bogey & Bailly 2007); the second was between a given azimuthal mode in both the velocity and the acoustic field. The latter approach has a theoretical motivation, detailed in § 3.2, and allows the determination of correlations between wavepackets in the flow and the radiated sound field.

As an evaluation of the errors in the present experiment, the TR-PIV results for the axial velocity at $x/D = 2$ for the $M = 0.4$ jet are compared in figure 4 to the measurements taken with the traversing Pitot tube and hot-wire. Close agreement is found for both the mean and r.m.s. values of the velocity.

The sampling frequency of 5 kHz was the maximum possible value with the available equipment. To evaluate the effect of aliasing in spectra obtained from the TR-PIV measurements, these are compared in figure 5 to hot-wire spectra. For positions close to the jet lipline, such as shown in figure 5(*b*,*c*), the difference between TR-PIV and hot-wire spectra is slight. Some discrepancies remain, and can be attributed to experimental uncertainty. However, on the jet axis (figure 5*a*) the difference becomes significant, particularly for frequencies far from the peak. We have evaluated the aliasing effect by downsampling the hot-wire signal to 5 kHz and then computing spectra. The result is shown in figure 5(*a*), and shows that part of the difference between TR-PIV and hot-wire spectra can be attributed to aliasing. However, in addition to the aliasing errors, inside the potential core the amplitudes of velocity fluctuations are much lower than in the regions of turbulent flow, leading to a reduction of the signal-to-noise ratio if one considers that the noise in PIV

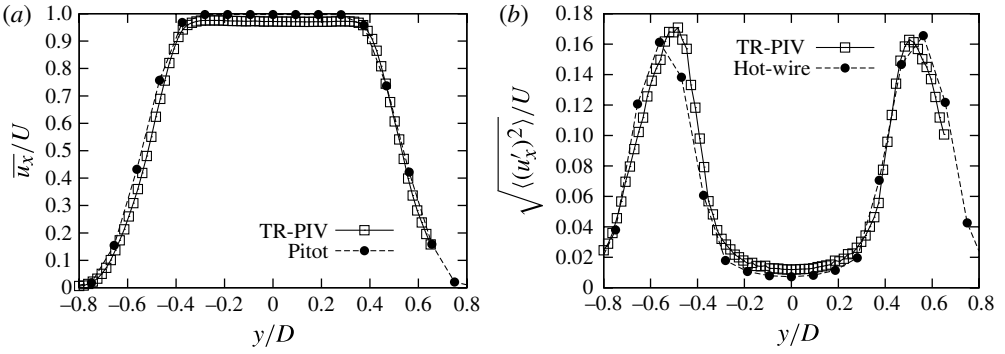

FIGURE 4. Comparison of (*a*) mean and (*b*) r.m.s. value of the axial velocity at $x/D = 2$ for the $M = 0.4$ jet using the different experimental techniques of the present work.

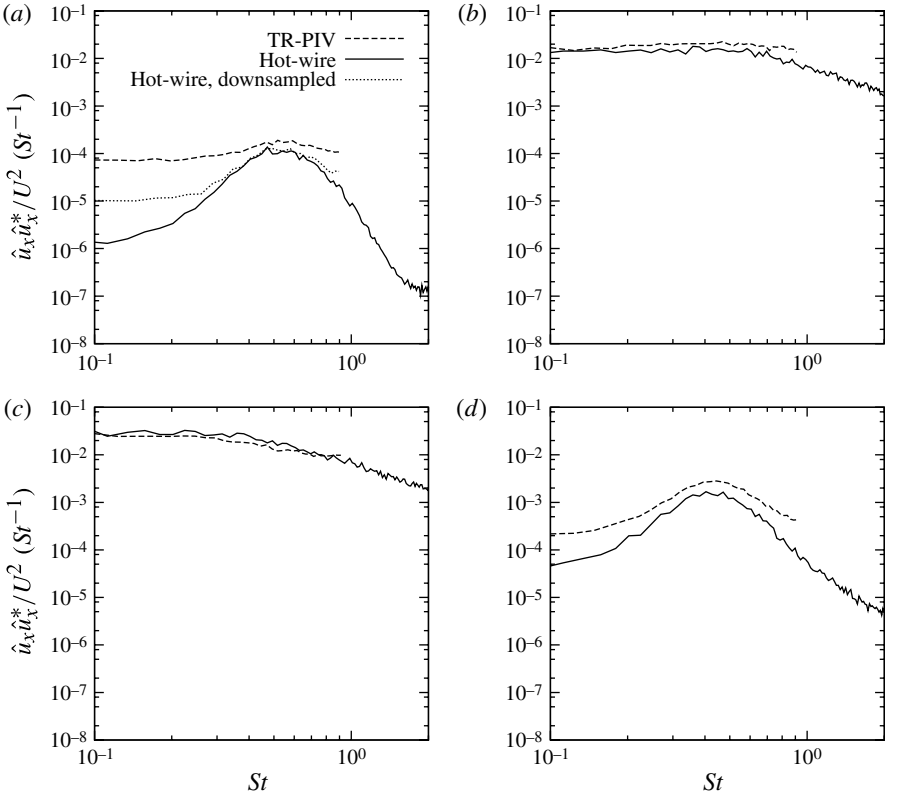

FIGURE 5. Comparison of hot-wire and PIV spectra for the $M = 0.4$ jet at (*a*) $x/D = 2$, $r/D = 0$, (*b*) $x/D = 2$, $r/D = 0.48$, (*c*) $x/D = 2$, $r/D = 0.57$ and (*d*) $x/D = 4$, $r/D = 0$.

measurements is uniformly distributed in space. In agreement with this, the errors in the determination of spectra from TR-PIV results are reduced for downstream positions on the jet centreline, as seen in figure 5(*d*).

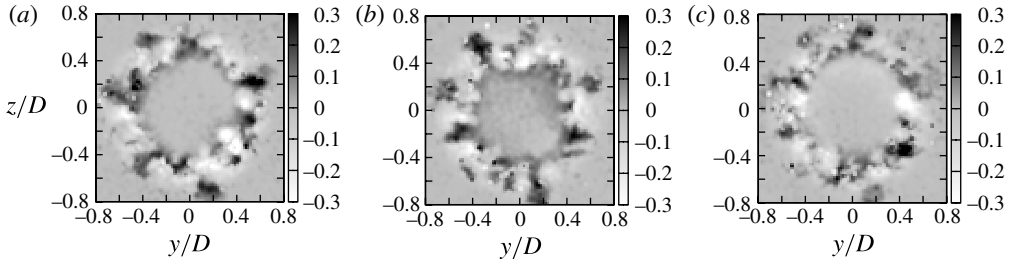

FIGURE 6. Sample instantaneous experimental axial velocity fluctuations u'_x/U at $x/D = 2$ for the Mach 0.4 jet.

To avoid significant errors due to aliasing in the TR-PIV results, we focus the analysis of the $M = 0.4$ jet measurements on the Strouhal number range of $0.3 \leqslant St \leqslant 0.7$. For higher Mach numbers, aliasing becomes significant even for this Strouhal number range; however, its effect is apparently uniform for all radial positions, as shown in the Appendix, where we see also that a correction of the PIV results based on hot-wire measurements leads to close agreement between velocity results for $M = 0.6$ and linear PSE solutions.

3. Azimuthal content of the velocity and acoustic fields

3.1. *Dominant azimuthal wavenumbers for velocity and far-field pressure*

Figure 6 shows snapshots of the instantaneous axial velocity fluctuations in a cross-section of the Mach 0.4 jet. Azimuthally coherent structures, such as those modelled by linear instability models, are hardly visible in this visualization, which is dominated by smaller-scale eddies whose characteristic length scale is small compared to the jet diameter. The jets are clearly not dominated by vortex rings such as are observed in forced (Crow & Champagne 1971; Hussain & Zaman 1981) or transitional jets (Becker & Massaro 1968; Violato & Scarano 2011), and at first sight it is not obvious that there exist wavepackets with low azimuthal wavenumber such as $m = 0$ or 1.

On the other hand, application of an azimuthal Fourier series to the turbulent field reveals that some energy is contained in the lower azimuthal modes, including the axisymmetric mode. Figure 7 shows the energy of the axial velocity fluctuations on the jet lipline, resolved as a function of the azimuthal wavenumber m. To obtain this, we decomposed the instantaneous time-resolved PIV results in an azimuthal Fourier series; the time series for each azimuthal mode of velocity, $\boldsymbol{u}(x, r, m, t)$, can then be used to compute the energies in figure 7. We note in figure 7(*a*) that the most energetic azimuthal mode is around 11 for the near-nozzle region ($x/D = 1$). As we move towards the end of the potential core ($x/D \approx 5.5$), lower azimuthal modes of velocity become more important, and the peak shifts to $m = 4$ for $x/D = 3$.

Rescaling of the azimuthal wavenumber with the local momentum thickness, δ_2, for each axial station, as in figure 7(*b*), shows that the peak azimuthal wavenumber scales with δ_2. The peak for $m\delta_2/r = 0.7$ is close to the results of Bogey, Marsden & Bailly (2011), who did large eddy simulations of $M = 0.9$ jets and found energy peaks at the nozzle exit for $m\delta_2/r \approx 0.8$. The scaling with the local momentum thickness is similar to what is observed in turbulent boundary layers; the results of Tomkins & Adrian (2005) show a peak for spanwise wavenumber of $k_z\delta_2 \approx 1$. Similar collapse of the energy distribution for the different azimuthal wavenumbers was shown by Tinney

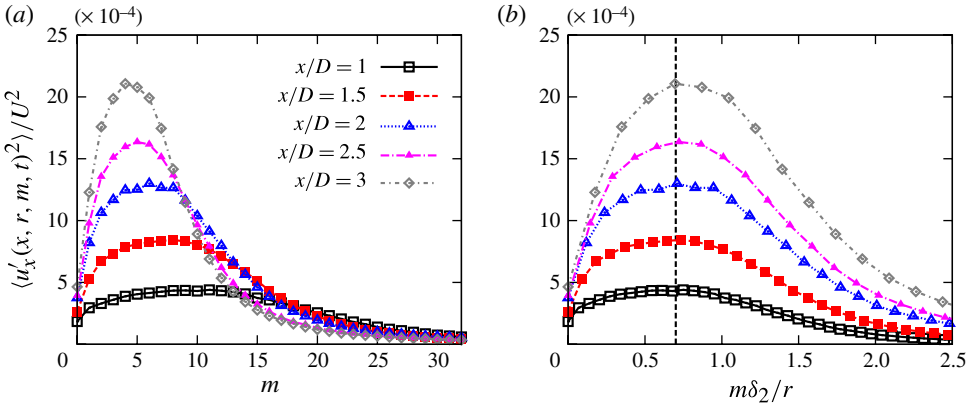

FIGURE 7. (Colour online) Energy of axial velocity fluctuations on the jet lipline as a function of azimuthal wavenumber scaled with (*a*) radius r and (*b*) local momentum thickness δ_2. The dashed line in (*b*) refers to $m\delta_2/r = 0.7$.

et al. (2008) for POD modes taken from cross-sections of a Mach 0.85 jet, but in that case the wavenumbers were scaled as mx/D. The similarities are probably due to the linear development of the mixing layer thickness with x/D; if δ_2/r is proportional to x/D the two representations are equivalent.

Presented in this way, the velocity field can be seen to comprise a number of scales of motion. The large-scale energy-containing structures have azimuthal coherence related to the local momentum thickness; but the energy for the lower azimuthal modes (e.g. $m = 0$ or 1) is not zero, despite their not being readily visible in an instantaneous visualization of the jet.

In contrast to the azimuthal structure of the velocity field, a number of experimental results (Maestrello 1976; Fuchs & Michel 1978; Juvé, Sunyach & Comte-Bellot 1979; Cavalieri *et al.* 2012) show that the radiated sound field at low polar angles is dominated by low azimuthal modes, especially for low frequencies. Figure 8 shows the far-field spectrum, at $\theta = 20°$, resolved into azimuthal modes for the present $M = 0.4$ jet; the acoustic field of this jet, and of the other jets studied in the present work, is documented in detail by Cavalieri *et al.* (2012). We see in figure 8(*a*) that for low angles the sound field is predominantly axisymmetric; this dominance of mode 0 is particularly significant for low Strouhal numbers, as exemplified by the sound pressure level for $St = 0.2$ shown in figure 8(*b*).

Theoretically, the different azimuthal organizations of the velocity and acoustic fields can be understood by noting that for low frequencies a condition of *radial compactness* is satisfied by the jet: the diameter is significantly lower than the acoustic wavelength. In such a situation, higher azimuthal modes will have low acoustic efficiency due to destructive azimuthal interference in the $\exp(im\phi)$ factor of the acoustic source.

Use of cylindrical coordinates and azimuthal Fourier modes in the integral solution of Lighthill's equation allows the quantification of this effect. For low acoustic angles, consideration of azimuthal mode m and frequency ω of the T_{xx} component of Lighthill's stress tensor leads to

$$p(R, \theta, m, \omega) = -\frac{\mathrm{i}^m k_a^2 \cos^2\theta \mathrm{e}^{-\mathrm{i}k_a R}}{2R} \int \mathrm{e}^{\mathrm{i}k_a x \cos\theta}\, \mathrm{d}x \int T_{xx}(x, r, m, \omega) \mathrm{J}_m(k_a r \sin\theta) r\, \mathrm{d}r, \quad (3.1)$$

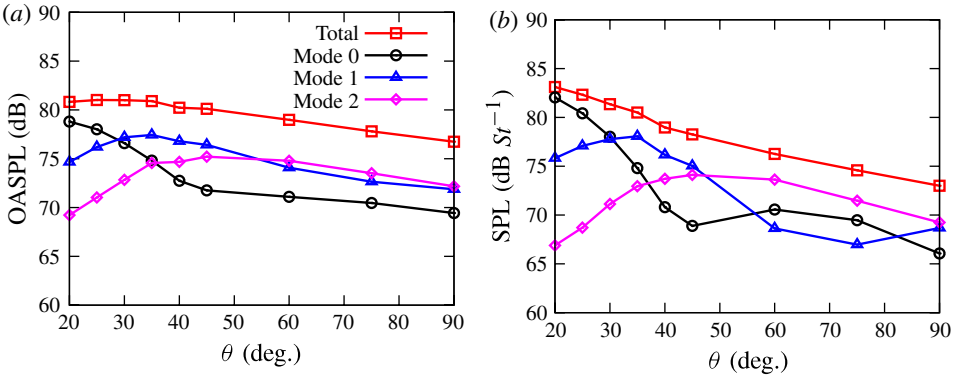

FIGURE 8. (Colour online) Directivity for the $M = 0.4$ jet: (a) overall sound and (b) SPL for $St = 0.2$. Taken from Cavalieri *et al.* (2012).

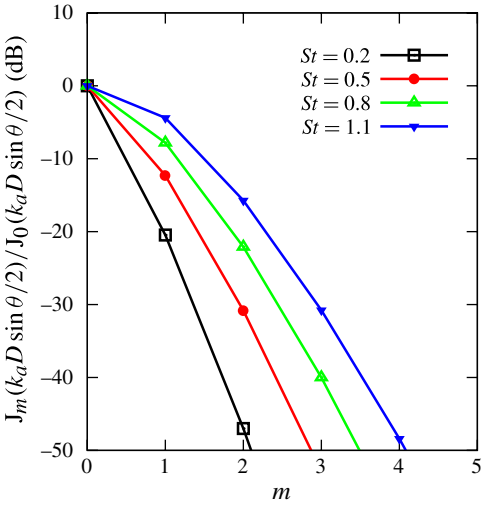

FIGURE 9. (Colour online) Acoustic efficiency for sound radiation at $\theta = 30°$ by the azimuthal mode m relative to the axisymmetric mode, for a ring source at $r = D/2$ in an $M = 0.6$ jet.

where k_a is the acoustic wavenumber ω/c. The Bessel function of the first kind, J_m, results from azimuthal integration, and leads to a lower efficiency of high azimuthal modes, as explored previously in the literature (Michalke 1970; Michalke & Fuchs 1975; Mankbadi & Liu 1984; Cavalieri *et al.* 2011).

This effect is illustrated in figure 9. Noting that $k_a r = 2\pi\, St\, Mr/D$, we see that the ordinate in the figure is the ratio of $\mathrm{J}_m(k_a r \sin\theta)$ to $\mathrm{J}_0(k_a r \sin\theta)$ in decibels, and indicates the efficiency of mode m relative to the axisymmetric mode for sound radiation at $\theta = 30°$. We note that for low Strouhal numbers this acoustic efficiency decays rapidly with increasing azimuthal wavenumber m, suggesting that low azimuthal modes in the turbulent field, despite their low energy, account for most of the sound generation at these low frequencies and polar angles.

It is well known that high-frequency sound tends to be refracted away from the jet axis, creating what is called a 'cone of silence', as demonstrated experimentally by Atvars, Schubert & Ribner (1965). These refraction effects are not explicitly modelled in Lighthill's analogy, and one may question its validity for sound radiation at shallow angles. However, low-frequency sound has lower refraction effects. In the experiment of Atvars *et al.* (1965), the lowest frequency studied in an $M = 0.3$ jet corresponds to $St \approx 0.2$, which is close to the spectral peak of jet noise at low angles. This frequency was found to lead to negligible refraction.

Accordingly, experiments with the present jets do not show a cone of silence for the low Strouhal numbers corresponding to the spectral peak, either for the overall sound or for the axisymmetric mode (see for instance the results in figure 8); and models of wavepacket radiation using (3.1) were successful in explaining the experimental directivity trends for azimuthal modes 0, 1 and 2 (Cavalieri *et al.* 2012). We consider thus that refraction effects are negligible for the low-frequency sound radiated at low axial angles, and use of (3.1) is appropriate in these conditions.

3.2. *Correlations between axisymmetric modes of velocity and far-field sound*

Motivated by the observed contrast between the azimuthal organization of the velocity and far-field pressure fields, and on the theoretical higher acoustic efficiency of lower azimuthal modes, we investigate the relationship between azimuthal modes in the jet and in the acoustic field by computing correlations between velocity and far-field pressure at $\theta = 20°$. We first present two-point correlations, defined as

$$C_{u_x,p}(x, r, R, \theta, \tau) = \frac{1}{t_f}\int_0^{t_f} u_x(x, r, \phi, t)p(R, \theta, \phi, t + \tau)\,\mathrm{d}t. \tag{3.2}$$

These correlations ignore the difference in the azimuthal content of the velocity and pressure fields, and amount to an attempt to correlate a high azimuthal wavenumber in the velocity field to a low one in the acoustic field.

If we assume, instead, a relationship between *azimuthal modes* in the velocity and the acoustic fields, such as in (3.1), it makes sense to correlate, rather, the axisymmetric modes of velocity and far-field pressure, as

$$C^0_{u_x,p}(x, r, R, \theta, \tau) = \frac{1}{t_f}\int_0^{t_f} u_x(x, r, m = 0, t)p(R, \theta, m = 0, t + \tau)\,\mathrm{d}t, \tag{3.3}$$

which isolates the axisymmetric mode of the axial velocity before correlation with the axisymmetric part of the far-field sound.

Results of the two-point correlations, as in (3.2), are presented in figures 10 and 11, for the $M = 0.4$ and $M = 0.6$ jets, respectively. Correlations were taken for $x/D = 4$ (upstream of the end of the potential core, as seen in figure 3), 5 (close to the end of the potential core) and 6 (downstream). For the correlations, the velocity was taken at $r = D/4$, and not on the jet lipline; as will be shown later, in figure 14, correlations tend to be higher for positions around this radial position. The correlation results have a typical noise level around 0.02. This is due to the reduced number of TR-PIV samples (19 414). We see that the two-point correlations in figures 10 and 11 are low, without an apparent peak above the noise level.

Computation of correlations between axisymmetric modes, as in (3.3), leads to the results shown in figures 12 and 13. The correlations are now well above the noise level, and are of order of 10 % for the $M = 0.6$ jet, which is significantly higher than values obtained by two-point correlations in previous studies of subsonic turbulent jets (see e.g. Schaffar 1979; Panda *et al.* 2005).

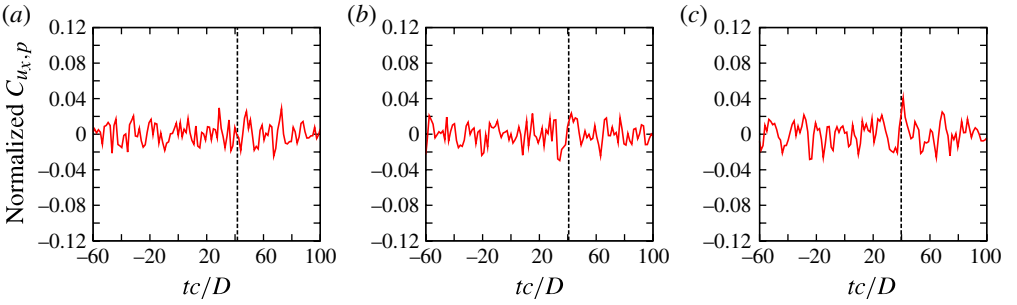

FIGURE 10. (Colour online) Two-point correlations for the $M = 0.4$ jet, taken with a velocity measurement at $r = D/4$ and far-field pressure at $\theta = 20°$: (*a*) $x/D = 4$, (*b*) $x/D = 5$, (*c*) $x/D = 6$. The dashed line indicates propagation time without flow–acoustic effects.

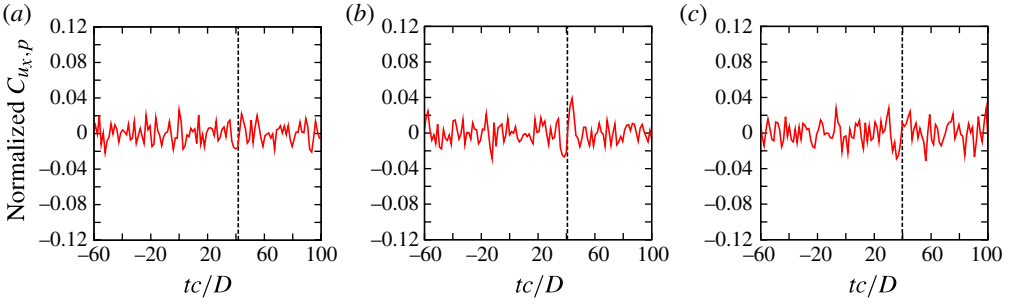

FIGURE 11. (Colour online) Two-point correlations for the $M = 0.6$ jet, taken with a velocity measurement at $r = D/4$ and far-field pressure at $\theta = 20°$: (*a*) $x/D = 4$, (*b*) $x/D = 5$, (*c*) $x/D = 6$. The dashed line indicates propagation time without flow–acoustic effects.

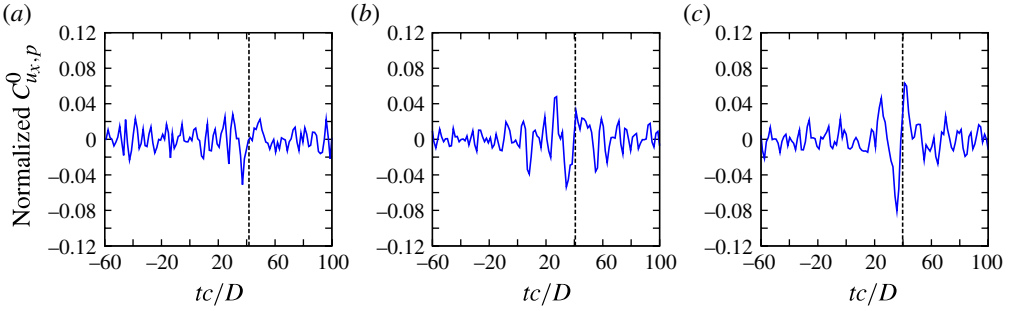

FIGURE 12. (Colour online) Correlations between mode-0 axial velocity at $r = D/4$ and mode-0 far-field pressure at $\theta = 20°$ for the $M = 0.4$ jet: (*a*) $x/D = 4$, (*b*) $x/D = 5$, (*c*) $x/D = 6$. The dashed line indicates average propagation time without flow–acoustic effects.

In addition, previous studies showed a strong decay of two-point correlations when the reference position is moved away from the jet centreline. In Panda *et al.*'s study, all correlations of subsonic jets taken at $r/D = 0.45$ were below the experimental

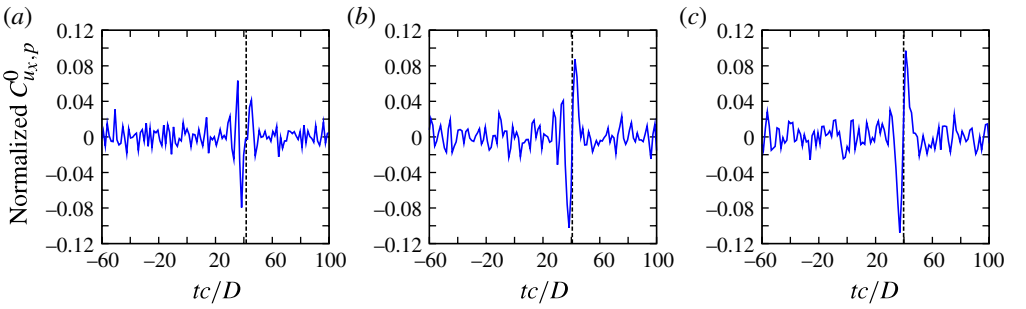

FIGURE 13. (Colour online) Correlations between mode-0 axial velocity at $r = D/4$ and mode-0 far-field pressure at $\theta = 20°$ for the $M = 0.6$ jet: (*a*) $x/D = 4$, (*b*) $x/D = 5$, (*c*) $x/D = 6$. The dashed line indicates average propagation time without flow–acoustic effects.

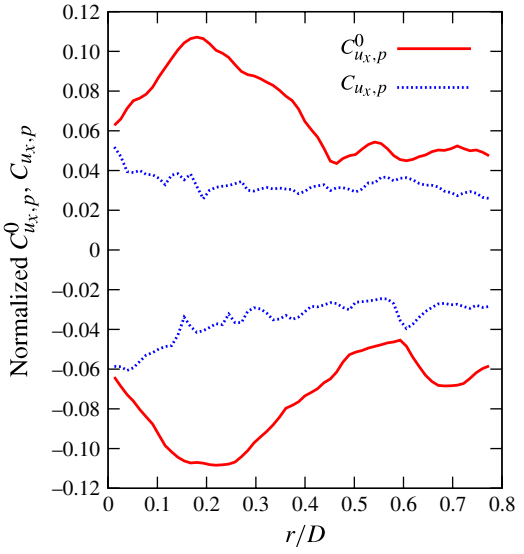

FIGURE 14. (Colour online) Maxima and minima of correlations between axial velocity far-field pressure for different radial positions. Results taken at the axial station $x/D = 6$ of the $M = 0.6$ jet.

noise level. When the axisymmetric velocity mode is considered we see significant correlations for several radial positions, as illustrated in figure 14, showing maxima and minima of correlations for both C and C^0. These correlations tend to the same value as the radius goes to zero, since the axial velocity on the centreline is constituted solely of mode 0 (further discussion will be presented in § 4.2). However, for higher r the two-point correlation C decays, and the maxima and minima are close to the noise level around 0.02 seen in figure 11. The correlation between axisymmetric modes C^0, on the other hand, does not decay, and is significantly greater than 0.02 for positions extending from the centreline to $r/D = 0.4$ or 0.5.

These results support the idea that the azimuthally coherent part of the velocity field has higher acoustic efficiency, and, despite being less energetic than the dominant

azimuthal wavenumbers, is the dominant source of low-angle sound radiation. However, care should be taken in the interpretation of these correlation results, since we see that correlations are significant over a region which is extended in both x and r; even when C^0 is used to account for individual azimuthal modes, the correlation is performed between a ring in the flow and a second ring in the acoustic field, and thus no information is obtained about the extended axial structure of the noise source. As will be shown in the next section, the axisymmetric mode of the velocity field compares favourably with a wavepacket model. In a wavepacket, sound radiation is the product of significant cancellation between axially distributed positive and negative parts. The radiated sound does not depend on a single, axially localized, ring in the flow; sound generation results from a delicate interference within the wavepacket (see discussion in Cavalieri *et al.* 2012). Hence, one should not expect correlations close to unity, even when these are performed between the respective azimuthal modes of velocity and pressure.

The observations in the present section motivate the research for an appropriate model for the lower-order azimuthal modes in a jet, which we develop in the next section as linear wavepackets.

4. Detection of wavepackets in the velocity field

Previous experimental observations of the present jets (Cavalieri *et al.* 2012) have shown that the measured acoustic radiation is compatible with a wave-like, non-compact source with low azimuthal wavenumber, and the results of the preceding section show further evidence linking the axisymmetric part of the velocity field and the radiated sound.

In the present section we investigate the lower azimuthal modes of the velocity field to ascertain if they can be modelled as wavepackets. For this we use as a reference solution a computation based on linear PSE (Herbert 1997) using the experimental mean field as a base flow. This is based on arguments given by Crighton & Gaster (1976) and Mankbadi & Liu (1981), who state that the large-scale perturbations of interest here only contain a small fraction of the total fluctuation energy and can thus be modelled as linear perturbations of the mean flow. The latter is established as the result of the nonlinear interactions between a wide range of temporal and spatial turbulent scales. Therefore, use of the mean field as a base flow implicitly accounts for most of the nonlinearity.

Most of the results of the present section refer to the $M = 0.4$ jet, since, due to the aliasing in the experiment, this is the most favourable case for comparison with TR-PIV results. Further comparisons with the $M = 0.5$ and $M = 0.6$ jets are shown in the Appendix.

4.1. *Linear parabolized stability equations (PSEs)*

Wavepackets in the jets were modelled using linear PSE, following the approach described by Gudmundsson & Colonius (2011). We describe the PSE approach briefly in the present section; more details can be found in the cited paper.

Parabolized stability equations represent a generalization of the parallel-flow linear stability theory for flows with a mild variation in the streamwise direction. For a free jet, the total flow field $\boldsymbol{q}$ is decomposed into a mean (time-averaged) and axisymmetric component $\bar{\boldsymbol{q}}$ and its fluctuations as $\boldsymbol{q}(\boldsymbol{x}, t) = \bar{\boldsymbol{q}}(\boldsymbol{x}) + \boldsymbol{q}'(\boldsymbol{x}, t)$, where $\boldsymbol{q} = [u_x, u_r, u_\phi, \rho, T]^{\mathrm{T}}$ is the vector of fluid variables and $\boldsymbol{x} = (x, r, \phi)$ are the coordinates on a cylindrical system. Based on the homogeneity of the mean flow

on the azimuthal direction and time, the fluctuating part can then be written as a sum of Fourier modes in the azimuthal direction and in frequency

$$\boldsymbol{q}'(\boldsymbol{x},t)=\sum_{\omega}\sum_{m=-M}^{M}\breve{\boldsymbol{q}}_{m,\omega}(x,r)\mathrm{e}^{\mathrm{i}m\phi}\mathrm{e}^{-\mathrm{i}\omega t}, \tag{4.1}$$

where $\breve{\boldsymbol{q}}_{m,\omega}$ is the modal function corresponding to the mode (m,ω).

The mean flow is a function of the axial and radial directions (x,r), but a slow variation of its properties along the axial direction is assumed. This assumption permits the decomposition of $\breve{\boldsymbol{q}}_{m,\omega}$ into a slowly varying shape function (that evolves in the same scale as the mean flow) and a rapidly varying wave-like part:

$$\breve{\boldsymbol{q}}_{m,\omega}(x,r)=A_{m\omega}(x)\tilde{\boldsymbol{q}}_{m,\omega}(x,r)=\exp\left(\mathrm{i}\int_{x}\alpha_{m,\omega}(\xi)\,\mathrm{d}\xi\right)\tilde{\boldsymbol{q}}_{m,\omega}(x,r). \tag{4.2}$$

Here $\alpha_{m,\omega}(x)$ is a complex axial wavenumber, for which a mild variation is also assumed. It is important to stress that the separation in scales between the mean flow and the modal shape functions on one hand, and the modal wavelengths associated with $\alpha_{m,\omega}$ on the other, is a necessary hypothesis in the derivation of the PSE. However, for low frequencies the wavelength can be comparable to the extent of the potential core.

We introduce the previous decomposition into the compressible Navier–Stokes, continuity and energy equations. After subtraction of the terms corresponding to the mean flow, and neglecting quadratic terms on the fluctuations, we arrive at the system of equations

$$(\boldsymbol{A}(\boldsymbol{q},\bar{\alpha},\omega)+\boldsymbol{B}(\bar{\boldsymbol{q}}))\;\tilde{\boldsymbol{q}}_{m,\omega}+\boldsymbol{C}(\bar{\boldsymbol{q}})\frac{\partial\tilde{\boldsymbol{q}}_{m,\omega}}{\partial x}+\boldsymbol{D}(\bar{\boldsymbol{q}})\frac{\partial\tilde{\boldsymbol{q}}_{m,\omega}}{\partial r}=\frac{1}{Re}\boldsymbol{E}\tilde{\boldsymbol{q}}_{m,\omega}. \tag{4.3}$$

The linear operators $\boldsymbol{A}$–$\boldsymbol{E}$ can be found in Gudmundsson & Colonius (2011). For brevity, the subscripts have been dropped from the shape function and wavenumber in the previous expression. The left-hand side in (4.3) is a linear spatial operator for the mode (m,ω), and each frequency-azimuthal mode component evolves independently of the others. Following from the slow axial variation assumed for $\tilde{\boldsymbol{q}}_{m,\omega}$, the second axial derivatives on the viscous terms are neglected, so that the system of equations can be integrated along the x-direction. The decomposition of (4.2) is ambiguous in that the spatial growth of $\breve{\boldsymbol{q}}_{m,\omega}$ can be absorbed into either the shape function $\tilde{\boldsymbol{q}}_{m,\omega}$ or the complex amplitude $A_{m,\omega}$ corresponding to the wave-like behaviour. Following Herbert (1997), the normalization condition

$$\int_{0}^{\infty}\tilde{\boldsymbol{q}}_{m,\omega}^{*}\frac{\partial\tilde{\boldsymbol{q}}_{m,\omega}}{\partial x}r\,\mathrm{d}r=0, \tag{4.4}$$

where the superscript $*$ denotes complex conjugation, is imposed individually on every mode, removing the exponential dependence on the shape function $\tilde{\boldsymbol{q}}_{m,\omega}$.

The characteristic boundary conditions of Thompson (1987) are used for the outer boundary, while centreline conditions are derived following Mohseni & Colonius (2000). The same approach of Gudmundsson & Colonius (2011) was applied to obtain numerical solutions of the system of equations (4.3). The reader is referred to that paper for further details on the computational method.

Adequate boundary conditions are required at the inlet, specifically for $\tilde{\boldsymbol{q}}_{m,\omega}$ and $\alpha_{m,\omega}$, for each mode. The complex amplitudes $A_{m,\omega}$ can be rescaled after the computations in order to fit experimental measurements, as linear PSE results are

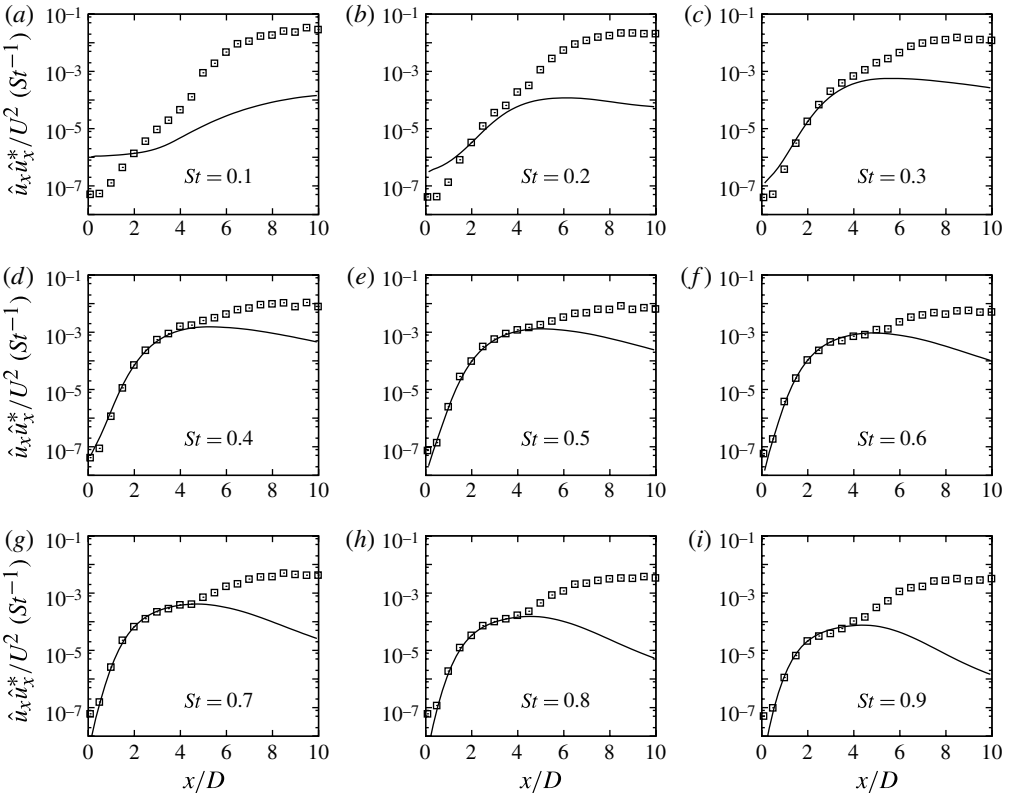

FIGURE 15. Comparison between linear PSE (lines) for $m = 0$ and experimental velocity fluctuations on the centreline (symbols) for the $M = 0.4$ jet. Subfigures (*a–i*) refer respectively to Strouhal numbers from 0.1 to 0.9 with increments of 0.1.

independent of the modal amplitudes and phases. A local spatial linear instability eigenvalue problem can be derived from the equation (4.3); from its solution, the dominant inflectional instability eigenmode is taken as initial condition for $\tilde{\boldsymbol{q}}_{m,\omega}$ and $\alpha_{m,\omega}$.

4.2. *Comparison with experimental velocity fluctuations on the jet centreline*

The linear modes have a free amplitude, and this has been adjusted using the velocity spectra on the jet centreline. There the kinematic boundary conditions are zero transverse velocity and finite axial velocity for azimuthal mode 0, zero axial velocity and finite transverse velocity for mode 1, and zero velocities for all higher modes (Batchelor & Gill 1962). As the velocity measurements were performed with a single hot-wire, we expect that in the potential core the measurements will be of the axial velocity, thus allowing the comparison between the mode 0 from linear PSE and the hot-wire spectra.

Figure 15 shows the comparison, between linear PSE and experiment, of the amplitude for the streamwise velocity component for the Mach 0.4 jet. The free constant multiplying linear PSE amplitudes was chosen by matching amplitudes at $x/D = 2$. Between the nozzle exit and the end of the potential core ($x/D \approx 5$–5.5) there is an amplification of four orders of magnitude of the fluctuation energy in

the experiment. In this region there is close agreement between linear PSE and experimental values for Strouhal numbers of 0.3–0.9.

We note in figure 15 differences between the modelled wavepackets and the experimental results for points downstream of the end of the potential core. Similar behaviour was also observed in previous work by Suzuki & Colonius (2006) and Gudmundsson & Colonius (2011). In these papers the discrepancies were attributed to fluctuations that were uncorrelated with the wavepackets at upstream positions. Proper orthogonal decomposition (POD) was applied to obtain modes correlated axially, and use of the first POD modes allowed uncorrelated oscillations to be filtered out, improving significantly the agreement at downstream positions. However, since the present hot-wire measurements are single-point we could not apply POD to these results to verify if this also applies to the current experiments.

For the two lower Strouhal numbers, 0.1 and 0.2, shown in figure 15(*a,b*), linear PSE underpredict the growth rate of the axisymmetric mode. This was also the case in other works (Suzuki & Colonius 2006; Gudmundsson & Colonius 2011) and, as shown in the Appendix, is also verified for the higher Mach numbers. These discrepancies have been attributed in the cited papers to increased non-parallel effects for these lower frequencies, since the potential core length becomes comparable to the wavelength for these Strouhal numbers, which invalidates the hypotheses in the PSE derivation shown in § 4.1.

The lack of agreement at low Strouhal numbers may also be due to nonlinear effects; such a possibility has been considered by Suponitsky, Sandham & Morfey (2010), who show in computations how the nonlinear interaction between waves at higher Strouhal numbers may affect the development of low-*St* velocity fluctuations and change the radiated sound field. The present results do not, however, allow us to discriminate between these two possibilities to explain the said discrepancies.

Similar agreement is found for the other jets over the same *St* range; this is shown in the Appendix. Due to the compressibility effects discussed by Cavalieri *et al.* (2012), the normalized amplitudes of the linear PSE modes on the jet centreline decrease as the Mach number is increased. This is shown in figure 16 for three Strouhal numbers. We note that the amplitudes near the nozzle exit are quite close, and lower growth rates due to compressibility lead to decreases in amplitudes for higher Mach numbers. The linear PSE modes are shown to correctly model these observed trends in the experimental fluctuations.

4.3. *Cross-stream planes*

Velocity measurements using time-resolved PIV in cross-stream planes of the jet allow application of a Fourier transform in time and of a Fourier series in azimuth, leading to a decomposition of the velocity field in both frequency and azimuthal wavenumber, such as in (4.1). This allows comparison of experiment with linear PSE results for each (ω, m) pair at several axial and radial positions.

We first show comparisons for the axisymmetric mode at $x/D = 2$ in § 4.3.1 to explain some of the general features of both the experiment and the PSE solution. The first helical mode is compared to linear PSE at the same axial station in § 4.3.2. Finally, the axial development of wavepackets is studied in § 4.3.3. All comparisons in the present section were made for the $M = 0.4$ jet.

Throughout this section, comparisons are restricted to the Strouhal number range of 0.3–0.7. Comparisons for Strouhal numbers of 0.1 and 0.2, not shown here, did not show good agreement with linear wavepacket models, similarly to what was verified for the hot-wire data in § 4.2.

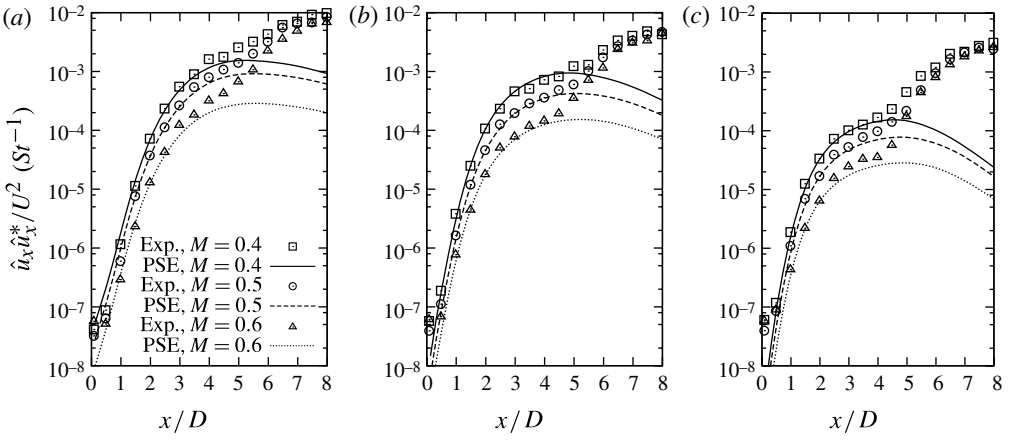

FIGURE 16. Compressibility effect in the velocity fluctuations and in the linear PSE amplitudes for (*a*) $St = 0.4$, (*b*) $St = 0.6$ and (*c*) $St = 0.8$.

4.3.1. *Axisymmetric mode at $x/D = 2.5$*

The stereoscopic TR-PIV results were compared to the radial shapes of the PSE solutions for azimuthal modes $m = 0$, 1. We begin the study of linear wavepackets by looking at the axisymmetric mode of the $M = 0.4$ jet in the present section, focusing first on jet cross-section at $x/D = 2.5$. In all comparisons of the axisymmetric mode obtained by TR-PIV results we have used the linear PSE results with amplitudes for u_x matched using the hot-wire spectra at $x/D = 2$ and $r/D = 0$; hence, no further adjustment was performed to match the PIV results. Figure 17 shows a comparison of the axial velocity fluctuations at this station for $m = 0$.

As seen in § 3.1, the fluctuation energy of the axisymmetric mode close to the jet lipline is much lower than the overall fluctuation energy, shown by dash-dotted lines in figure 17. This is in contrast to the jet centreline, where all axial velocity fluctuations correspond, as expected, to the axisymmetric mode.

The comparison in figure 17 between PSE and experimental mode 0 shows fairly good agreement. However, the PSE solution presents nearly zero amplitudes at a radial position close to the lipline (the precise position depends on the frequency). To understand the meaning of this zero amplitude, we see in figure 18 a comparison of the phase between experiment and linear PSE for Strouhal number of 0.7. We note that in the experiment there is a phase jump close to π between the two sides of the mixing layer, a behaviour also recovered by the PSE solution.

This phase opposition for the streamwise velocity is found in coherent, axisymmetric vortical structures obtained by phase averages of forced jets (Hussain & Zaman 1981; Cohen & Wygnanski 1987; Petersen & Samet 1988), and was also seen previously in unforced jets by Lau, Fisher & Fuchs (1972). An illustration of such structures is shown in figure 18(*b*). At the radial position of the centre of a vortex, shown with a dashed line, the axial velocity fluctuation is zero; therefore, a forced jet consisting mostly of periodic vortex rings presents a near-zero amplitude for the streamwise velocity at the radial position of the vortex centres. We can conjecture that the jitter of coherent structures in an unforced jet will lead to temporal changes in the radial position of the centres, so that the experimental amplitude is not zero, as sketched in figure 18(*c*).

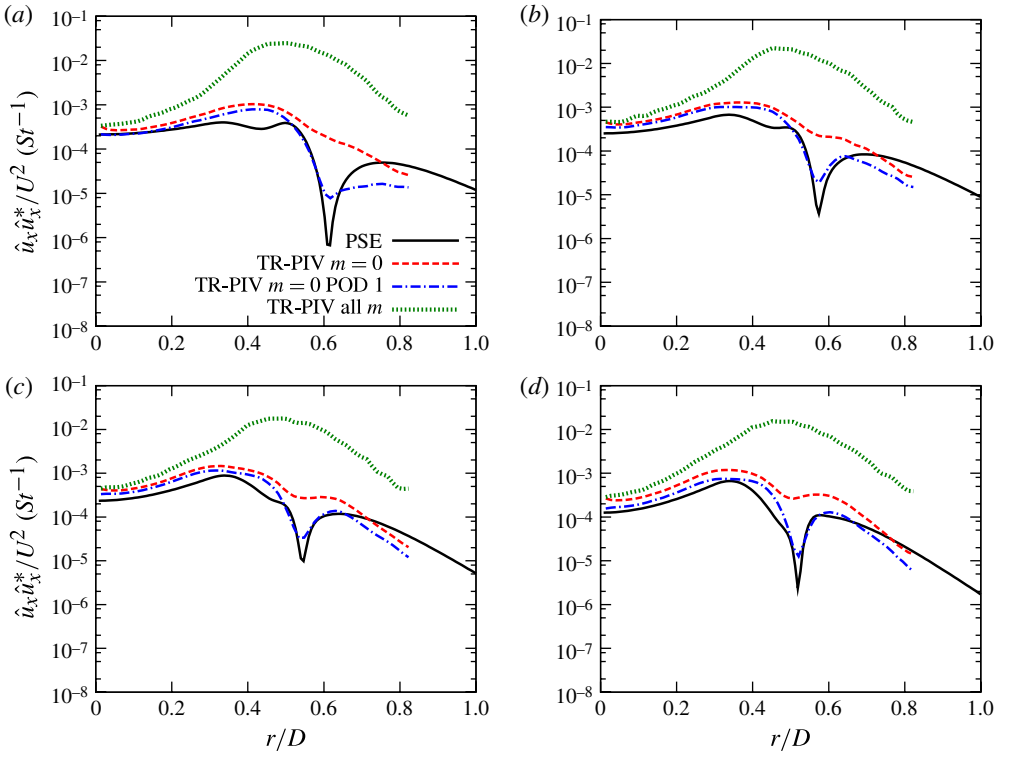

FIGURE 17. (Colour online) Comparison between u_x from linear PSE and experiment for $m = 0$, $M = 0.4$ and $x/D = 2.5$: (*a*) $St = 0.4$, (*b*) $St = 0.5$, (*c*) $St = 0.6$, (*d*) $St = 0.7$.

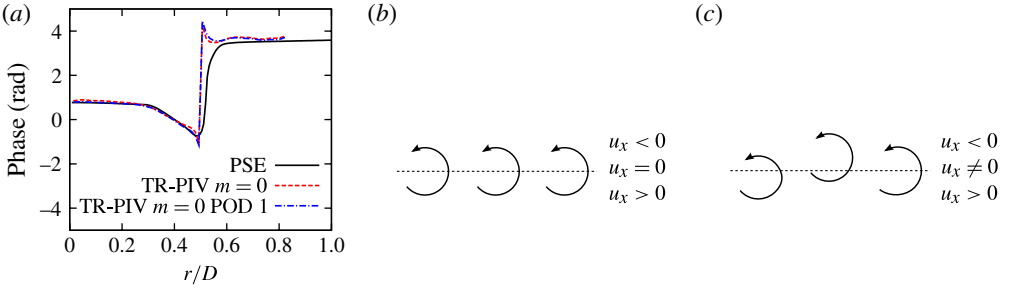

FIGURE 18. (Colour online) (*a*) Phases of the streamwise velocity for the axisymmetric mode at $St = 0.7$ and $x/D = 2.5$. (*b*) Sketch representing the phase difference across a mixing layer with a developing Kelvin–Helmholtz instability. (*c*) Effect of jitter in the position of vortex centres.

Based on this conjecture, in an attempt to obtain an average structure of the streamwise velocity without jitter, we apply spectral POD in the radial direction to extract the correlated part of the fluctuations, using the same approach described by Jung, Gamard & George (2004), which amounts to solving the integral equation

$$\int R_{i,j}(x, r, r', m, \omega)\xi_j(x, r', m, \omega)r'\,\mathrm{d}r' = \lambda(x, m, \omega)\xi_i(x, r, m, \omega), \tag{4.5}$$

where ξ is an eigenfunction (POD mode), λ is the corresponding eigenvalue and $R_{i,j}$ is given by

$$R_{i,j}(x, r, r', m, \omega) = u_i(x, r, m, \omega)u_j^*(x, r', m, \omega). \tag{4.6}$$

This kernel $R_{i,j}(x, r, r', m, \omega)r$ is not Hermitian; an auxiliary Hermitian kernel was obtained, as in Jung *et al.* (2004), by multiplying the integral equation (4.5) by $\sqrt{r}$ and considering $R_{i,j}(x, r, r', m, \omega)\sqrt{r'r}$ as the kernel and $\xi_i(x, r, m, \omega)\sqrt{r'}$ as the eigenfunction.

POD is calculated numerically using the approach described by Delville (1995), with a single $3N \times 3N$ matrix formed by computation of $R_{i,j}$ for the three velocity components using the N points in the radial direction.

Throughout this section we use the projection of the experimental results onto the mode with highest energy, obtained by

$$\mathrm{POD}(u) = \sqrt{\lambda^{(1)}}\xi^{(1)}, \tag{4.7}$$

where $\lambda^{(1)}$ is the highest eigenvalue and $\xi^{(1)}$ the corresponding eigenfunction. This projection was used to extract the coherent part of the velocity field, and is referred to as the 'first POD mode' throughout the remainder of this paper.

The x component of the first POD mode is plotted in figures 17 and 18, where we see that this mode indeed presents an amplitude close to zero near the lipline, at the position of the phase jump. The position of this zero amplitude agrees closely with the PSE solution, as shown in figure 17.

The radial velocity is compared in figure 19. Note that linear PSE solutions have the same free constant multiplying all flow variables; therefore, no further adjustment is done for this comparison. The agreement between linear PSE and experiment is good, especially considering the first POD mode close to the centreline. Since the radial velocity should be zero on the centreline for $m = 0$, the present results suggest that POD acts in this case as a filter, removing some of the uncorrelated noise in the experimental results and leading to the correct trend for the radial velocity close to the centreline.

4.3.2. *First helical mode at $x/D = 2.5$*

As in the axisymmetric case, linear PSE solutions have a free constant that is determined using experimental data. However, since the hot-wire measurements of axial velocity on the centreline cannot give information about helical modes, we have used the TR-PIV results at $x/D = 2.5$ to determine this free amplitude for $m = 1$. We define an inner product

$$\begin{aligned}\langle \boldsymbol{u}(x, r, \omega, m), \breve{\boldsymbol{u}}(x, r, \omega, m)\rangle = \int_0^{r_f} \big[u_x(x, r', \omega, m)\breve{u}_x^*(x, r', \omega, m) \\ + u_r(x, r', \omega, m)\breve{u}_r^*(x, r', \omega, m) + u_\phi(x, r', \omega, m)\breve{u}_\phi^*(x, r', \omega, m)\big]\, r'\, \mathrm{d}r'\end{aligned} \tag{4.8}$$

between the experimental results and the linear PSE solutions, where r_f is the maximum radius available from the PIV measurements, and $\breve{\boldsymbol{u}}$ refers to the velocity modelled by the PSE solution $\breve{\boldsymbol{q}}_{m,\omega}$. If the velocity field can be expressed as

$$\boldsymbol{u}(x, r, \omega, m) = b(x, \omega, m)\breve{\boldsymbol{u}}(x, r, \omega, m), \tag{4.9}$$

the value of b can be determined as

$$b(x, \omega, m) = \frac{\langle \boldsymbol{u}(x, r, \omega, m), \breve{\boldsymbol{u}}(x, r, \omega, m)\rangle}{\|\breve{\boldsymbol{u}}(x, r, \omega, m)\|^2}. \tag{4.10}$$

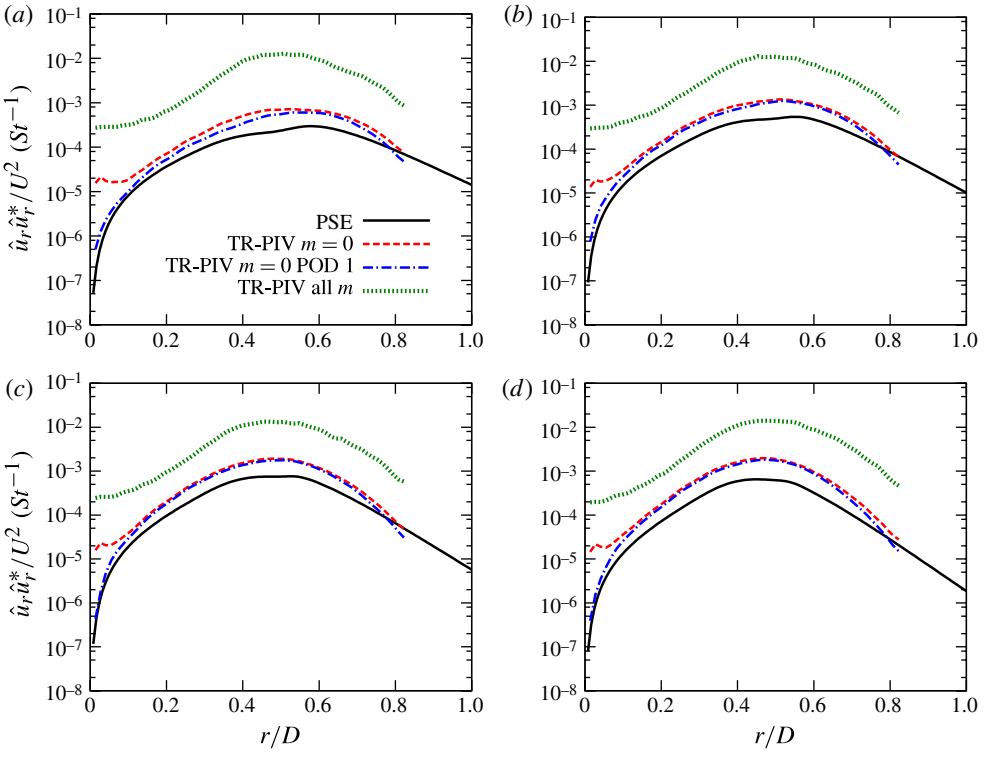

FIGURE 19. (Colour online) Comparison between u_r from linear PSE and experiment for $m = 0$, $M = 0.4$ and $x/D = 2.5$: (*a*) $St = 0.4$, (*b*) $St = 0.5$, (*c*) $St = 0.6$, (*d*) $St = 0.7$.

We use the results at $x/D = 2$ to determine b $(x = 2D, \omega, m)$, and use this value of b as the free constant multiplying the linear PSE results for all values of x and r.

Figure 20 presents comparisons for the axial velocity at $x/D = 2$. The radial velocity in the same axial station is compared in figure 21. We note that, as for the axisymmetric mode, for all but the $St = 0.7$ results, the solution of the linear PSE presents a near-zero amplitude close to the jet lipline, which compares favourably with the first POD mode calculated from the experimental data. The agreement between model and experiment is good for both the axial and radial velocity components. A somewhat worse agreement for $St = 0.7$ may be related to the lower amplification of this frequency. Linear PSE are expected to provide good predictions for significantly amplified modes.

4.3.3. *Axial development of wavepackets*

We illustrate the development of wavepackets in the jet by comparing the linear PSE solution for Strouhal number 0.5 to the experimental results for both the axisymmetric and first helical modes at axial stations ranging from $x/D = 1$ to $x/D = 8$. This comparison is shown for the axisymmetric mode in figure 22 for the axial velocity, and in figure 23 for the radial velocity fluctuations.

We see in figures 22 and 23 three distinct zones in the jet with regard to the wavepacket development. In a first region, exemplified by the results at $x/D = 1$ and $x/D = 1.5$, the velocity fluctuations present some differences from linear PSE, suggesting that this near-nozzle region is characterized by a transition from the

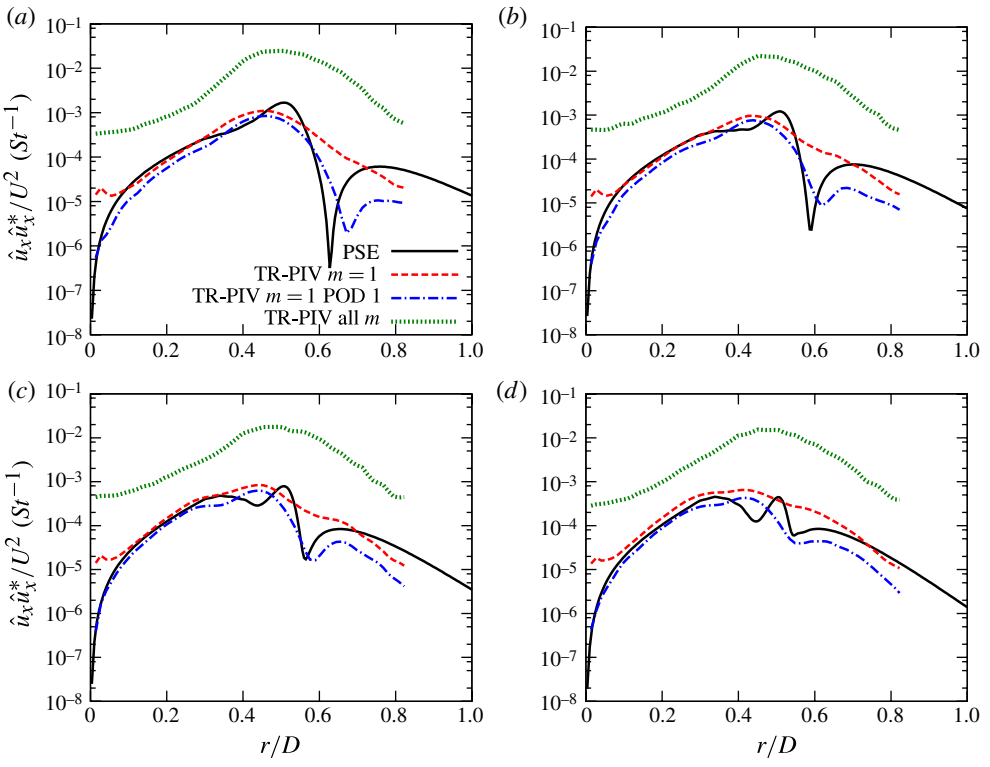

FIGURE 20. (Colour online) Comparison between u_x from linear PSE and experiment for $m = 1$, $M = 0.4$ and $x/D = 2.5$: (*a*) $St = 0.4$, (*b*) $St = 0.5$, (*c*) $St = 0.6$, (*d*) $St = 0.7$.

fluctuations internal to the nozzle to the Kelvin–Helmholtz mode observed downstream. This transition is more clearly seen in the fluctuations close to the jet lipline; on the centreline, the flow seems to conform earlier to a jet instability, at, say, $x/D = 0.5$, as seen in the hot-wire results in § 4.2. Another possibility to explain results for low x is that in this region wavepackets are indeed present, but do not dominate the velocity fluctuations, especially close to the lipline.

Between $x/D = 2$ and the end of the potential core ($x/D \approx 5.5$ for the $M = 0.4$ jet) the velocity fluctuations are closely matched by linear PSE, for both axial and radial velocity fluctuations, albeit with what seems to be a systematic underestimation of the velocity amplitudes. This is possibly due to aliasing errors in the TR-PIV results; note that velocity from the linear PSE was scaled using hot-wire spectra on the jet centreline, and the TR-PIV spectra in this region, as shown in figure 5, tend to overestimate the energies due to aliasing. This overestimation is nearly uniform for all radial positions. This is shown in the Appendix for the $M = 0.6$ jet, which presents more aliasing effects than the $M = 0.4$ case; when differences between hot-wire and PIV spectra are discounted the agreement is significantly improved.

However, for locations downstream of the end of the potential core, the agreement between the wavepacket model and the experiment becomes progressively worse, as exemplified by the results for $6 \leqslant x/D \leqslant 8$. This could be due to nonlinear interactions that become significant due to the amplitude growth of fluctuations with increasing x/D, invalidating the assumptions of linear PSE; if this is the case, nonlinear PSE

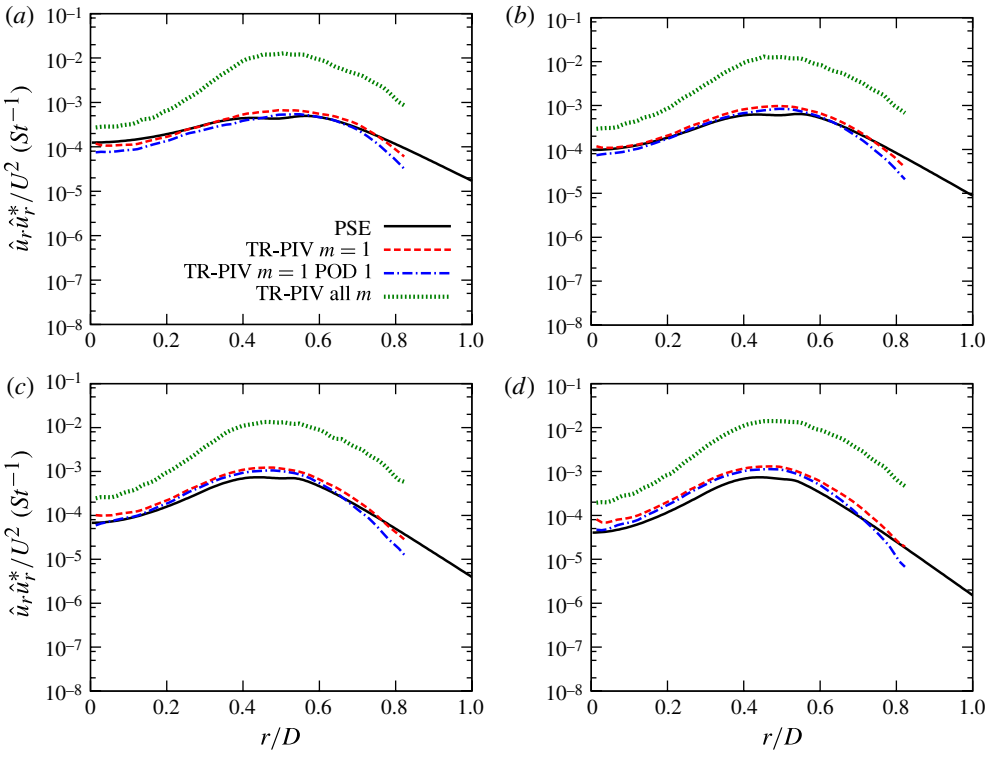

FIGURE 21. (Colour online) Comparison between u_r from linear PSE and experiment for $m = 1$, $M = 0.4$ and $x/D = 2.5$: (*a*) $St = 0.4$, (*b*) $St = 0.5$, (*c*) $St = 0.6$, (*d*) $St = 0.7$.

could improve the agreement with the experiment for higher x/D. However, a second possibility is that linear wavepackets are still present at downstream stations, but account only for a small part of the azimuthally coherent overall energy; radial POD is, in this case, no longer an efficient means by which to extract wavepackets from the PIV data. We favour this second hypothesis based on the agreement previously obtained by Suzuki & Colonius (2006) and Gudmundsson & Colonius (2011) between linear stability and the near pressure field; the axial POD used in those works led to close agreement at positions significantly downstream of the end of the potential core. The use of an axial POD is not feasible with the present experimental setup, since separate measurements were taken for each value of x/D. Moreover, preliminary comparisons of the measured near-field pressure of the present jets with linear PSE led to good agreement up to $x/D = 8.9$, which is well beyond the end of the potential core (Breakey *et al.* 2013).

Results representing the development of wavepackets for the helical mode at $St = 0.5$ are shown in figures 24 and 25, for the axial and radial velocity components, respectively. We observe an overall picture similar to the $m = 0$ results; however, for $m = 1$ the discrepancies between linear PSE and experiment start to become significant for $x/D \approx 4$ for the axial velocity (the radial velocity presents fairly good agreement up to $x/D = 5$).

To present these results, and also comparisons for other Strouhal numbers, in a more compact manner, we use the inner product defined in (4.8) to define a metric, β,

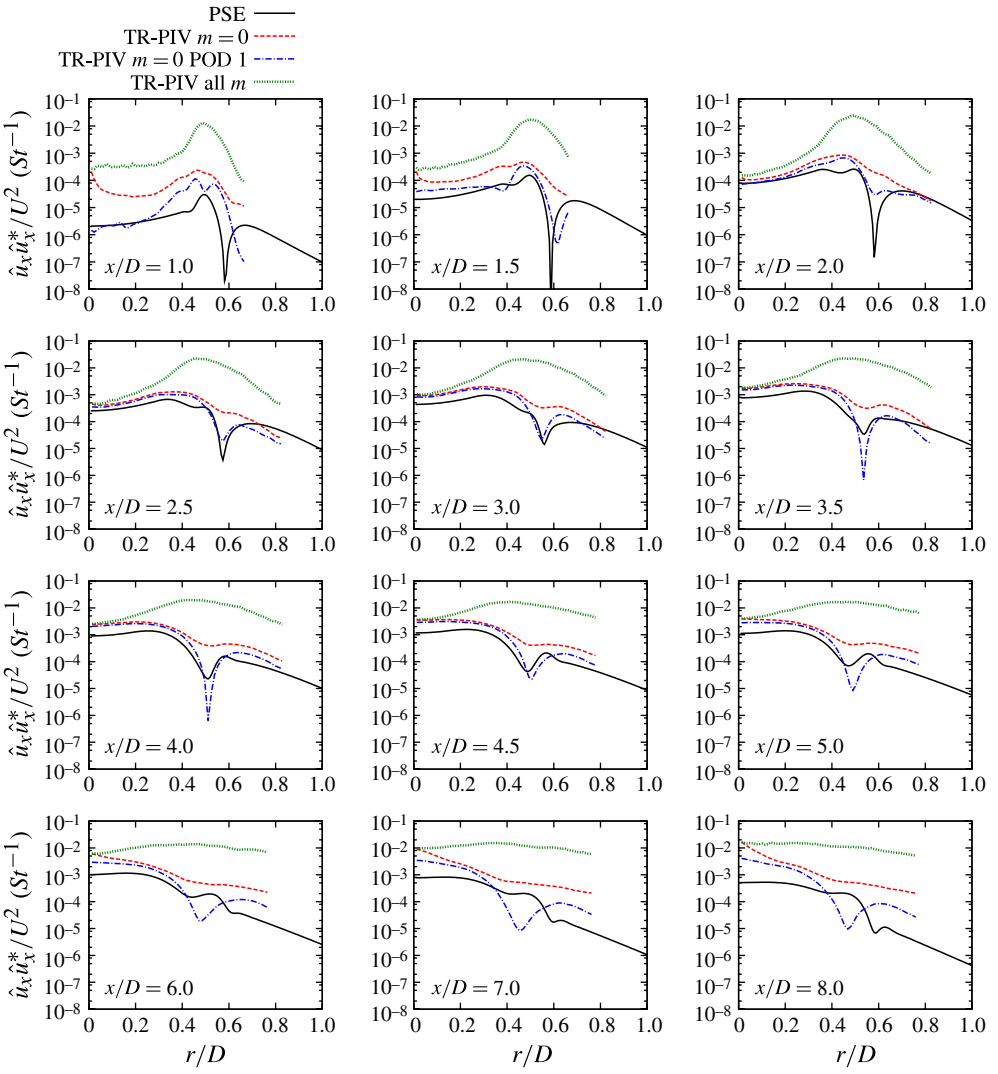

FIGURE 22. (Colour online) Comparison between u_x from linear PSE and experiment for $m=0$, $M=0.4$ and $St=0.5$: $x/D=1$, 1.5, 2, 2.5, 3, 3.5, 4, 4.5, 5, 6, 7, 8.

of the agreement between linear PSE and experiment, similar to what is done by Gudmundsson & Colonius (2011). If we define

$$\beta(x,\omega,m)=\frac{\langle \boldsymbol{u}(x,r,\omega,m),\breve{\boldsymbol{u}}(x,r,\omega,m)\rangle}{\|\boldsymbol{u}(x,r,\omega,m)\|\,\|\breve{\boldsymbol{u}}(x,r,\omega,m)\|} \tag{4.11}$$

we have $0\leqslant|\beta|\leqslant 1$, where $|\beta(x,\omega,m)|=1$ means that linear PSE and experiment have exactly the same radial shapes for the three velocity components for given axial station, frequency and azimuthal mode. On the other hand, $|\beta(x,\omega,m)|=0$ indicates orthogonality between model and experiment. Since this metric is an inner product normalized by the amplitudes in both PSE and experiment, a high value of β indicates only agreement between radial shapes of the three velocity components.

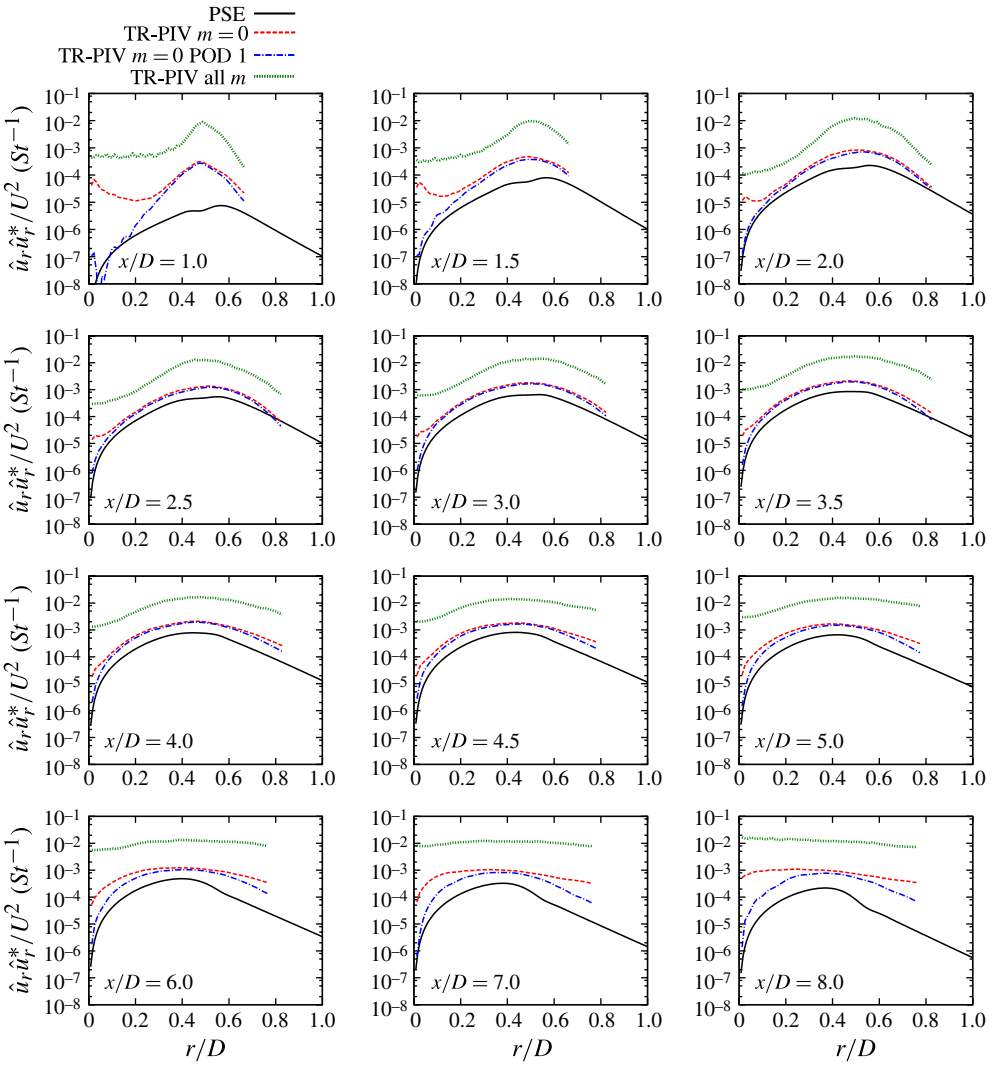

FIGURE 23. (Colour online) Comparison between u_r from linear PSE and experiment for $m=0$, $M=0.4$ and $St=0.5$: $x/D=1$, 1.5, 2, 2.5, 3, 3.5, 4, 4.5, 5, 6, 7, 8.

The β metric was calculated using the full velocity data. Results of the metric $|\beta|$ are shown in figure 26(*a*,*b*), for azimuthal modes 0 and 1, respectively.

Good agreement is obtained for both the axisymmetric and the first helical mode, as illustrated by values of $|\beta|$ equal to 0.9 and higher. The results in figure 26 show in all cases the three regions discussed above. In an initial region, agreement is not good; this is followed by a region upstream of the end of the potential core with close agreement between PSE and experiment, and at downstream positions discrepancies between model and experiment become significant.

On the other hand, we note that the values of β are *frequency-dependent*. Wavepackets with high St tend to match experimental results better for low x, and the opposite happens at downstream positions, where agreement with low St is better. This trend is consistent with the growth rates expected for each axial station. For low

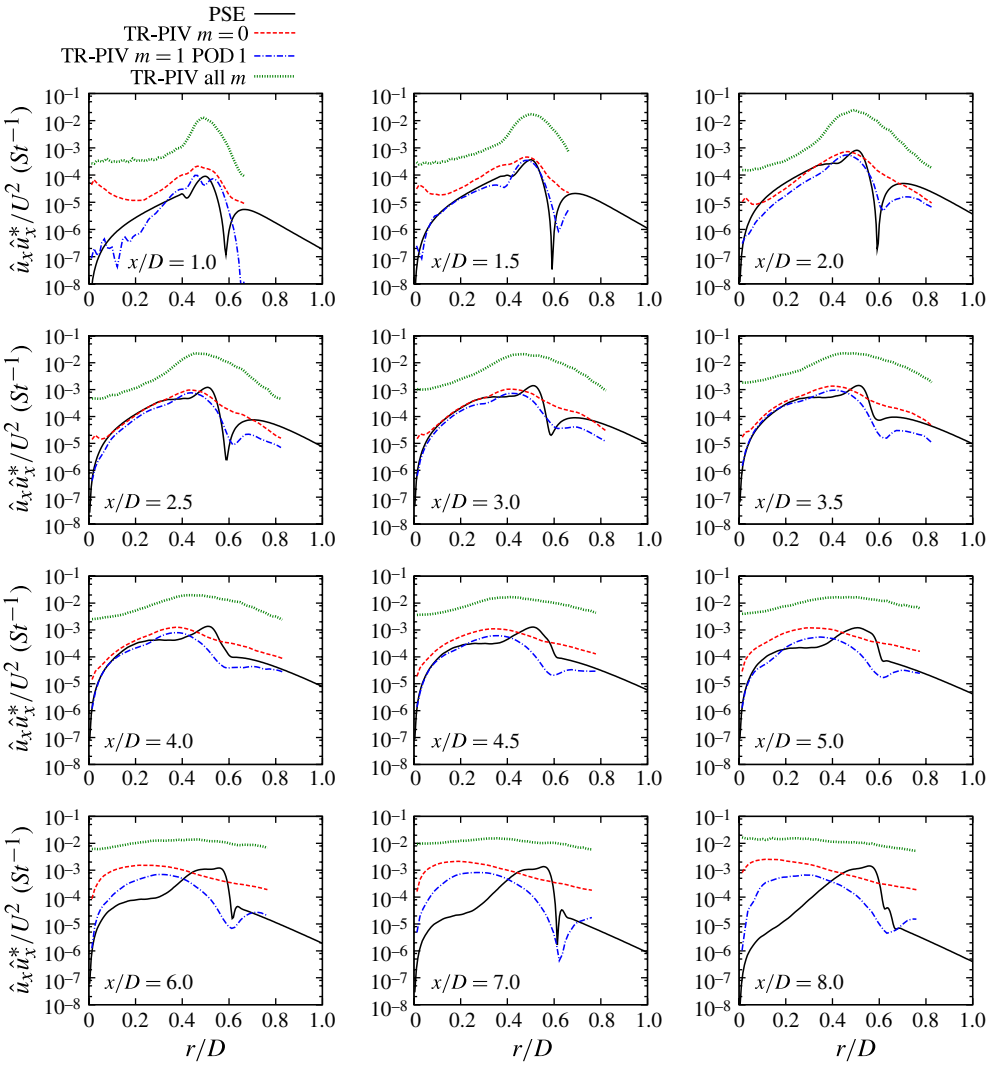

FIGURE 24. (Colour online) Comparison between u_x from linear PSE and experiment for $m = 1$, $M = 0.4$ and $St = 0.5$: $x/D = 1$, 1.5, 2, 2.5, 3, 3.5, 4, 4.5, 5, 6, 7, 8.

values of x/D, the relatively thinner mixing layer will lead to a high frequency for maximum growth rate, and wavepackets with high St will have a fast spatial growth near the nozzle exit. They thus tend to dominate the early development of the overall fluctuations for a given frequency and azimuthal mode, while low-St waves, with lower growth rate, take longer to have a significant contribution to the measured velocity fluctuations.

This situation is reversed downstream, since the velocity profile becomes progressively stable to high Strouhal numbers, whereas waves with low St are amplified over a longer extent of the jet. The decay of the high-frequency disturbances suggests that the velocity field is no longer dominated, in the downstream region, by wavepackets with high Strouhal number. The downstream persistence of low-frequency waves may explain their better agreement with the experimental results.

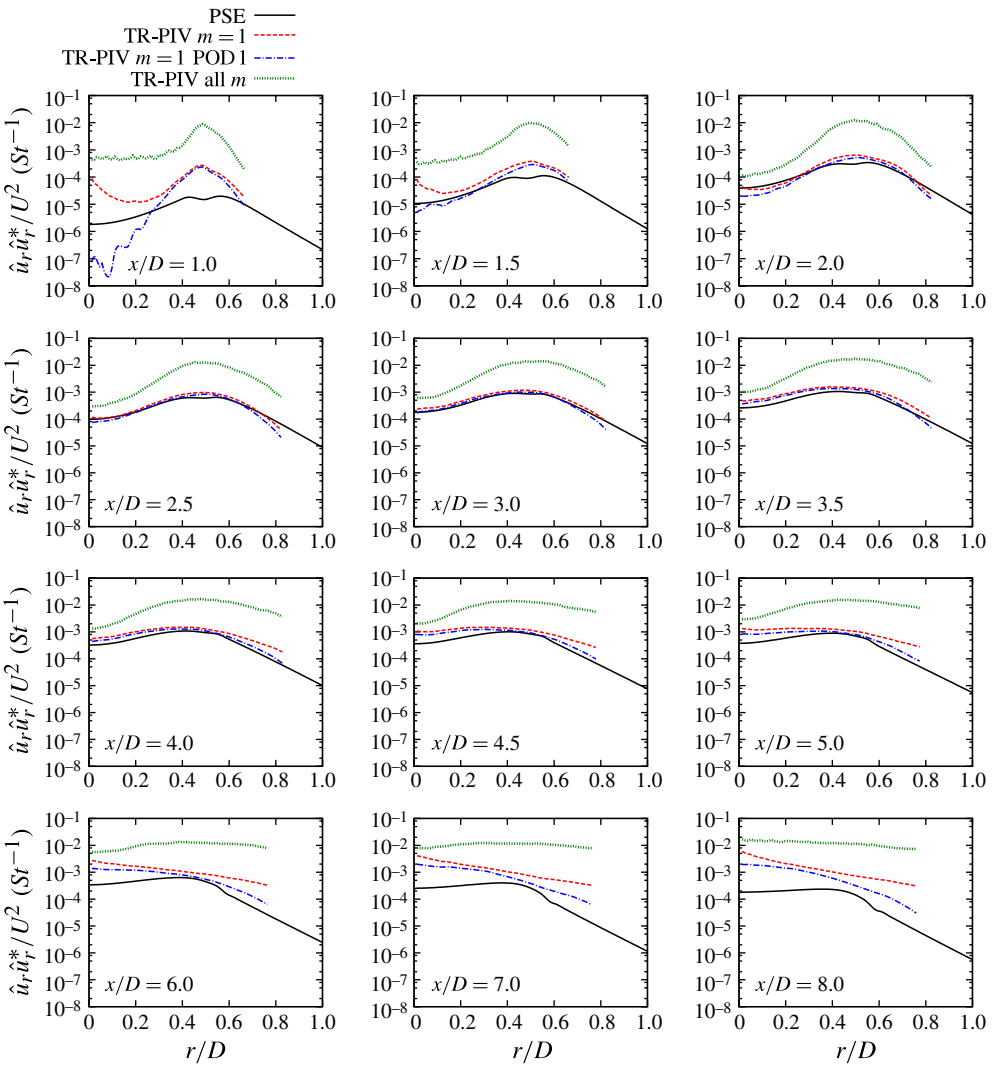

FIGURE 25. (Colour online) Comparison between u_r from linear PSE and experiment for $m=1$, $M=0.4$ and $St=0.5$: $x/D=1$, 1.5, 2, 2.5, 3, 3.5, 4, 4.5, 5, 6, 7, 8.

5. Conclusion and perspectives

We present a study of velocity fluctuations in turbulent subsonic jets without externally imposed forcing, time-resolved measurements allowing the simultaneous extraction of azimuthal modes in the flow and in the acoustic field. The velocity field is seen to present significant energy for high azimuthal wavenumbers, whereas low-angle radiation is predominantly axisymmetric. On the other hand, the axisymmetric mode of the velocity field has non-zero amplitude, and when this is isolated from the turbulence and correlated to the far-field sound, correlations of the order of 10 % are obtained, values significantly higher than the two-point correlations obtained for these jets and other experiments in the literature.

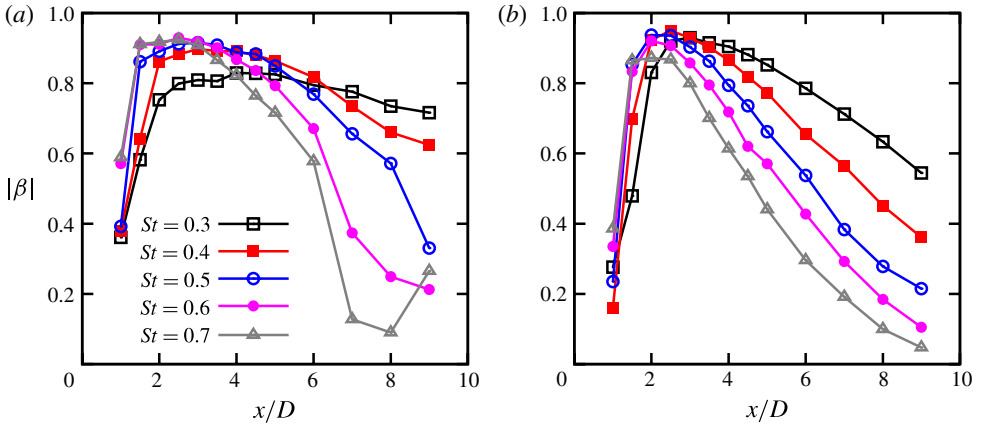

FIGURE 26. (Colour online) Absolute value of normalized inner product between linear PSE and experiment for (*a*) $m = 0$ and (*b*) $m = 1$.

The velocity field is then studied to verify whether this axisymmetric structure, and also the first helical mode, can be described as a superposition of wavepackets. Linear PSE are used for this, providing a wavepacket model accounting for the slow divergence of the experimental mean velocity profiles. There is good agreement for azimuthal modes 0 and 1 until the end of the potential core, showing that linear wavepackets are an appropriate model for the development of fluctuations in such flows, and that these modes present a wavepacket structure, in agreement with source models identified using far-field information (Kœnig *et al.* 2011*a*; Papamoschou 2011; Cavalieri *et al.* 2012).

The agreement found between linear PSE and the experimental velocity fluctuations constitutes further support of the contention that the fluctuations in turbulent jets, for low Strouhal numbers and azimuthal wavenumbers, can be described as linear wavepackets with the mean field used as a base flow, at least until the end of the potential core. Some nonlinearity is nonetheless implicit, since the base flow in the computations is the experimental mean field. The background turbulence can be seen to establish this mean field via the Reynolds stresses; this base flow now supports a linear Kelvin–Helmholtz instability leading to an extended hydrodynamic wavepacket.

The linearity of the velocity fluctuations contrasts with some numerical studies for low Reynolds number jets (Mohseni, Colonius & Freund 2002; Suponitsky *et al.* 2010), which show that nonlinear effects are necessary to describe the evolution of near-field disturbances. In these transitional flows, most of the kinetic energy of fluctuations is related to azimuthally coherent structures formed during laminar–turbulent transition; the high amplitudes of these structures leads to nonlinear effects in the wavepacket evolution, even close to the nozzle exit. However, as seen in § 3.1, for a high Reynolds number jet with a turbulent boundary layer in the nozzle, as in the present case, only a small fraction of the turbulent kinetic energy is contained in the low azimuthal modes, which favours application of a linear approach.

The present results show that a part of the turbulent field of high Reynolds number jets can be obtained using the Navier–Stokes equations linearized using the mean velocity field. This is quite different from the general view of turbulence as an essentially nonlinear phenomenon. We doubt, though, that the dominant turbulent

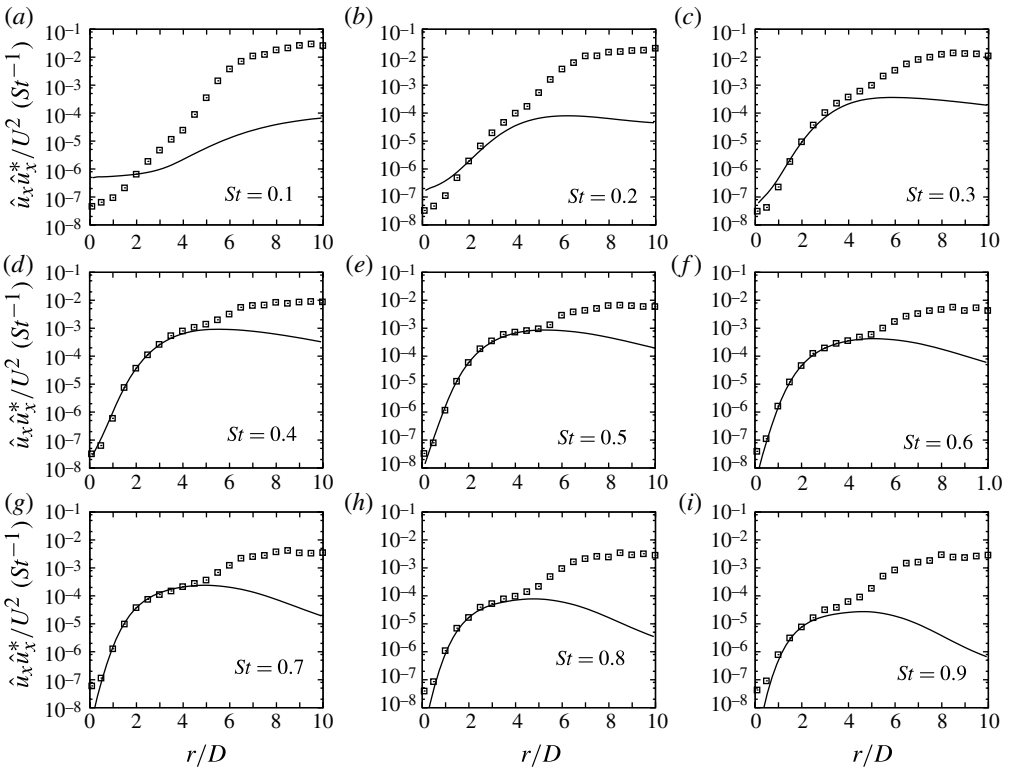

FIGURE 27. Comparison between linear PSE (lines) for $m = 0$ and experimental velocity fluctuations on the centreline (symbols) for the $M = 0.5$ jet. Subfigures (*a–i*) refer respectively to Strouhal numbers from 0.1 to 0.9 with increments of 0.1.

velocity fluctuations, of high azimuthal wavenumber, could be obtained with similar linearizations. On the other hand, if we are looking for the significant velocity fluctuations for sound generation, which have significantly lower energy, a linear wavepacket model appears to be appropriate to describe the evolution from the nozzle exit to the end of the potential core, at least in a statistical sense: we note that all comparisons between linear PSE and experiment were done using averaged spectra to obtain amplitudes and phases for each frequency and azimuthal mode. Linear PSE are thus seen to be a good model for a statistical description of large-scale structures.

Downstream of the end of the potential core, though, the model differs from the experimental results. We believe the discrepancy is at least in part the result of the very small contribution of the organized wavepacket to the overall fluctuation energy, and a failure of the radial POD to extract this low-energy structure. Simultaneous acquisition of several axial planes of data may be required to educe the wavepacket in this region.

Acknowledgements

We thank C. Fourment-Cazenave, P. Braud and Dr J. Delville for their work during the experiments. We also thank Drs K. Gudmundsson, A. Samanta and A. Sinha for

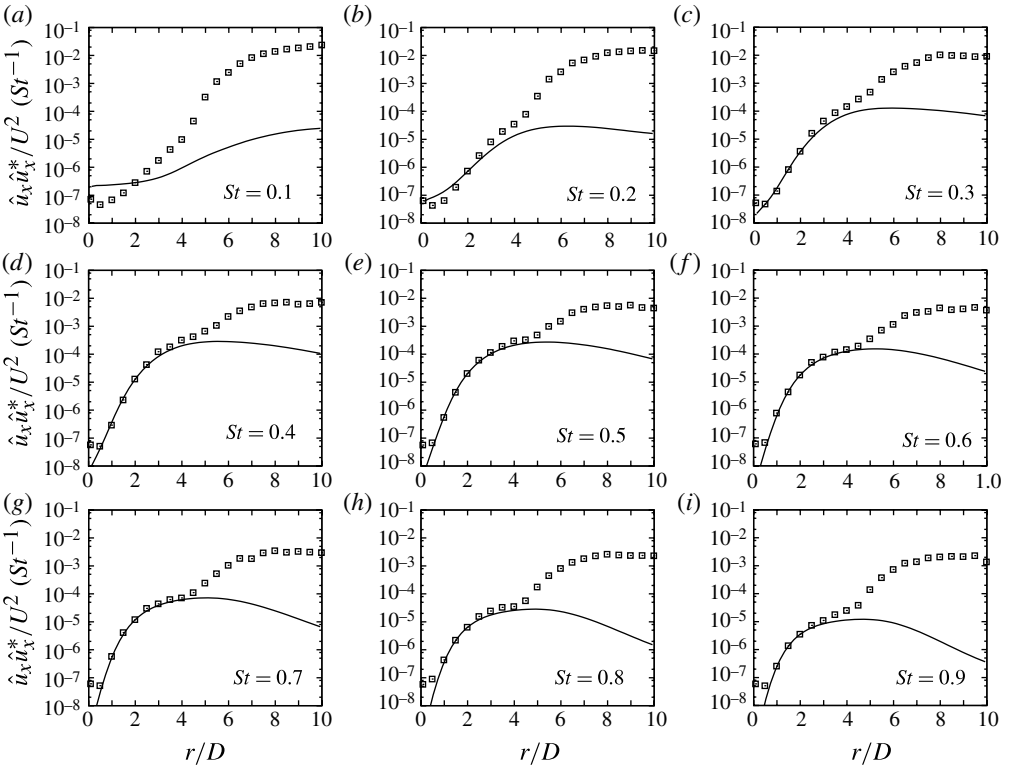

FIGURE 28. Comparison between linear PSE (lines) for $m = 0$ and experimental velocity fluctuations on the centreline (symbols) for the $M = 0.6$ jet. Subfigures (a–i) refer respectively to Strouhal numbers from 0.1 to 0.9 with increments of 0.1.

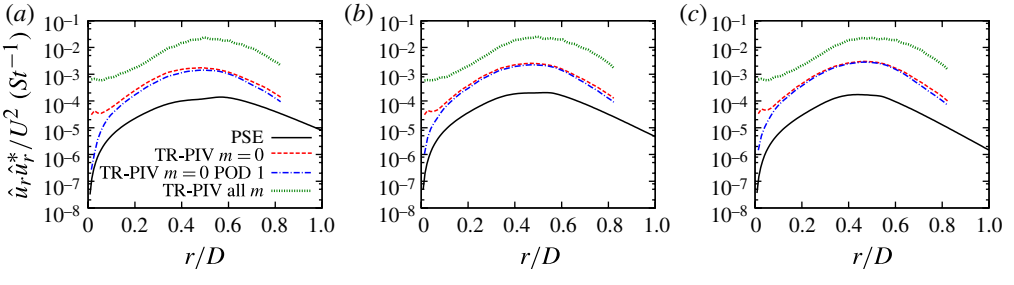

FIGURE 29. (Colour online) Comparison between u_r from linear PSE and experiment for $m = 0$, $M = 0.6$ and $x/D = 3$: (a) $St = 0.4$, (b) $St = 0.5$, (c) $St = 0.6$.

their contributions on the development of the PSE code. This work was supported by CNPq, National Council of Scientific and Technological Development, Brazil, and through the EU–Russian programme ORINOCO (FP7-AAT-2010-RTD-Russia; project number 266103). D.R. acknowledges funding by the EU Marie Curie COFUND programme. T.C. acknowledges support from the US Navy Naval Air Systems Command (NAVAIR) with Dr J. Spyropoulos as technical monitor.

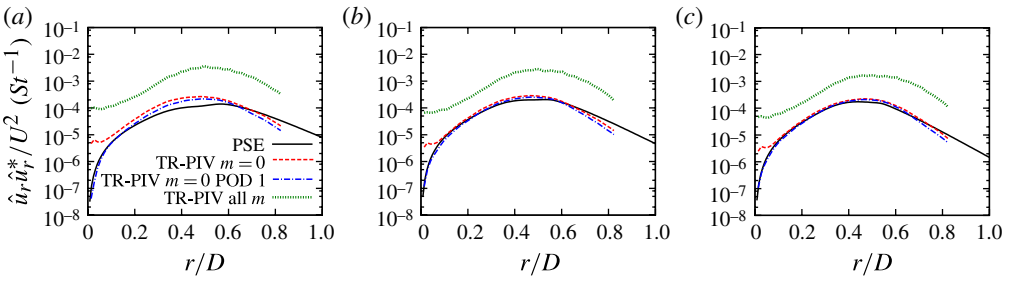

FIGURE 30. (Colour online) Comparison between u_r from linear PSE and experiment (with aliasing correction) for $m = 0$, $M = 0.6$ and $x/D = 3$: (*a*) $St = 0.4$, (*b*) $St = 0.5$, (*c*) $St = 0.6$.

Appendix. Linear PSE comparisons for Mach 0.5 and 0.6

We show in figures 27 and 28 the comparison between the axisymmetric mode obtained with linear PSE and the experimental results for the axial velocity fluctuations on the jet centreline, respectively, for the $M = 0.5$ and 0.6 jets.

The observed trends for both jet Mach numbers are quite similar to the results for the $M = 0.4$ jet shown in figure 15. For Strouhal numbers between 0.3 and 0.9 there is close agreement between PSE and the experiment until the end of the potential core. Discussion of the possible reasons for the discrepancies at lower frequencies is presented in § 4.2.

For comparison using the TR-PIV results, increasing the jet Mach number leads to higher aliasing, since the sampling rate was fixed at 5 kHz for all experiments. As a result, the spectral estimates using TR-PIV are significantly higher than the corresponding hot-wire results.

As an example of this effect, figure 29 presents comparisons at $x/D = 3$ for the axisymmetric mode of the radial velocity for the $M = 0.6$ jet. The radial shape of the PSE solution agrees closely with the first POD mode of the experiment. The measured amplitudes are higher than the PSE solution fitted with hot-wire spectra, but this amplitude change seems to be constant with radius.

We have performed an *ad hoc* correction for aliasing by defining a multiplicative constant for each frequency, which was obtained by dividing the hot-wire spectra on the jet centreline by the TR-PIV spectral estimate for u_x at the same position. This same constant was applied to all radial positions. Results are shown in figure 30. The amplitudes are now quite close, indicating that the shifts in figure 29 are indeed related to aliasing in the experiments for high Mach number.

REFERENCES

ARMSTRONG, R. R., FUCHS, H. V. & MICHALKE, A. 1977 Coherent structures in jet turbulence and noise. *AIAA J.* **15**, 1011–1017.

ATVARS, J., SCHUBERT, L. K. & RIBNER, H. S. 1965 Refraction of sound from a point source placed in an air jet. *J. Acoust. Soc. Am.* **37** (1), 168–170.

BATCHELOR, G. K. & GILL, A. E. 1962 Analysis of the stability of axisymmetric jets. *J. Fluid Mech.* **14** (4), 529–551.

BECKER, H. A. & MASSARO, T. A. 1968 Vortex evolution in a round jet. *J. Fluid Mech.* **31** (3), 435–448.

BOGEY, C. & BAILLY, C. 2007 An analysis of the correlations between the turbulent flow and the sound pressure fields of subsonic jets. *J. Fluid Mech.* **583**, 71–97.

BOGEY, C., MARSDEN, O. & BAILLY, C. 2011 Large-eddy simulation of the flow and acoustic fields of a Reynolds number 105 subsonic jet with tripped exit boundary layers. *Phys. Fluids* **23**, 035104.

BREAKEY, D. E. S., JORDAN, P., CAVALIERI, A. V. G., LÉON, O., ZHANG, M., LEHNASCH, G., COLONIUS, T. & RODRÍGUEZ, D. 2013 Near-field wavepackets and the far-field sound of a subsonic jet. In *19th AIAA/CEAS Aeroacoustics Conference, Berlin, Germany*, AIAA Paper 2013-2083.

CAVALIERI, A. V. G., JORDAN, P., AGARWAL, A. & GERVAIS, Y. 2011 Jittering wave-packet models for subsonic jet noise. *J. Sound Vib.* **330** (18–19), 4474–4492.

CAVALIERI, A. V. G., JORDAN, P., COLONIUS, T. & GERVAIS, Y. 2012 Axisymmetric superdirectivity in subsonic jets. *J. Fluid Mech.* **704**, 388–420.

COHEN, J. & WYGNANSKI, I. 1987 The evolution of instabilities in the axisymmetric jet. Part 1. The linear growth of disturbances near the nozzle. *J. Fluid Mech.* **176**, 191–219.

CRIGHTON, D. G. & GASTER, M. 1976 Stability of slowly diverging jet flow. *J. Fluid Mech.* **77** (2), 397–413.

CROW, S. C. 1972 Acoustic gain of a turbulent jet. In *Phys. Soc. Meeting, Univ. Colorado, Boulder, paper IE*, vol. 6.

CROW, S. C. & CHAMPAGNE, F. H. 1971 Orderly structure in jet turbulence. *J. Fluid Mech.* **48** (3), 547–591.

DELVILLE, J. 1995 La décomposition orthogonale aux valeurs propres et l'analyse de l'organisation tridimensionnelle des écoulements turbulents cisaillés libres. PhD thesis, Université de Poitiers.

FUCHS, H. V. & MICHEL, U. 1978 Experimental evidence of turbulent source coherence affecting jet noise. *AIAA J.* **16** (9), 871–872.

GUDMUNDSSON, K. & COLONIUS, T. 2011 Instability wave models for the near-field fluctuations of turbulent jets. *J. Fluid Mech.* **689**, 97–128.

HERBERT, T. 1997 Parabolized stability equations. *Annu. Rev. Fluid Mech.* **29** (1), 245–283.

HUSSAIN, A. K. M. F. & ZAMAN, K. B. M. Q. 1981 The 'preferred mode' of the axisymmetric jet. *J. Fluid Mech.* **110**, 39–71.

JORDAN, P. & COLONIUS, T. 2013 Wave packets and turbulent jet noise. *Annu. Rev. Fluid Mech.* **45** (1), 173–195.

JUNG, D., GAMARD, S. & GEORGE, W. K. 2004 Downstream evolution of the most energetic modes in a turbulent axisymmetric jet at high Reynolds number. Part 1. The near-field region. *J. Fluid Mech.* **514**, 173–204.

JUVÉ, D., SUNYACH, M. & COMTE-BELLOT, G. 1979 Filtered azimuthal correlations in the acoustic far field of a subsonic jet. *AIAA J.* **17**, 112–113.

JUVÉ, D., SUNYACH, M. & COMTE-BELLOT, G. 1980 Intermittency of the noise emission in subsonic cold jets. *J. Sound Vib.* **71**, 319–332.

KERHERVÉ, F., JORDAN, P., CAVALIERI, A. V. G., DELVILLE, J., BOGEY, C. & JUVÉ, D. 2012 Educing the source mechanism associated with downstream radiation in subsonic jets. *J. Fluid Mech.* **710**, 606–640.

KŒNIG, M. 2011 Réduction de bruit de jet par injection fluidique en corps central tournant. PhD thesis, Université de Poitiers.

KŒNIG, M., CAVALIERI, A. V. G., JORDAN, P., DELVILLE, J., GERVAIS, Y. & PAPAMOSCHOU, D. 2013 Farfield filtering and source imaging of subsonic jet noise. *Journal of Sound and Vibration* **332** (18), 4067–4088.

KŒNIG, M., FOURMENT-CAZENAVE, C., JORDAN, P. & GERVAIS, Y. 2011*b* Jet noise reduction by fluidic injection from a rotating plug. In *17th AIAA/CEAS Aeroacoustics Conference, Portland, OR, USA*.

LAU, J. C., FISHER, M. J. & FUCHS, H. V. 1972 The intrinsic structure of turbulent jets. *J. Sound Vib.* **22** (4), 379–384.

LAUFER, J. & YEN, T.-C. 1983 Noise generation by a low-Mach-number jet. *J. Fluid Mech.* **134**, 1–31.

LEE, H. K. & RIBNER, H. S. 1972 Direct correlation of noise and flow of a jet. *J. Acoust. Soc. Am.* **52**, 1280–1290.

LIGHTHILL, M. J. 1952 On sound generated aerodynamically. Part 1. General theory. *Proc. R. Soc. Lond.* A 564–587.

MAESTRELLO, L. 1976 Two-point correlations of sound pressure in the far field of a jet: experiment. NASA Tech. Rep. TM X-72835.

MANKBADI, R. & LIU, J. T. C. 1981 A study of the interactions between large-scale coherent structures and fine-grained turbulence in a round jet. *Phil. Trans. R. Soc. Lond.* A **298** (1443), 541–602.

MANKBADI, R. & LIU, J. T. C. 1984 Sound generated aerodynamically revisited: large-scale structures in a turbulent jet as a source of sound. *Phil. Trans. R. Soc. Lond.* A **311** (1516), 183–217.

MICHALKE, A. 1970 A wave model for sound generation in circular jets. *Tech. Rep.*, Deutsche Luft- und Raumfahrt.

MICHALKE, A. 1971 Instabilität eines kompressiblen runden Freistrahls unter Berücksichtigung des Einflusses der Strahlgrenzschichtdicke. *Z. Flugwiss.* **19**, 319–328, English translation, NASA TM 75190, 1977.

MICHALKE, A. & FUCHS, H. V. 1975 On turbulence and noise of an axisymmetric shear flow. *J. Fluid Mech.* **70**, 179–205.

MOHSENI, K. & COLONIUS, T. 2000 Numerical treatment of polar coordinate singularities. *J. Comput. Phys.* **157**, 787–795.

MOHSENI, K., COLONIUS, T. & FREUND, J. B. 2002 An evaluation of linear instability waves as sources of sound in a supersonic turbulent jet. *Phys. Fluids* **14**, 3593.

MOORE, C. J. 1977 The role of shear-layer instability waves in jet exhaust noise. *J. Fluid Mech.* **80** (2), 321–367.

ÖSTERLUND, J. M., JOHANSSON, A. V., NAGIB, H. M. & HITES, M. H. 2000 A note on the overlap region in turbulent boundary layers. *Phys. Fluids* **12** (1), 1–4.

PANDA, J., SEASHOLTZ, R. G. & ELAM, K. A. 2005 Investigation of noise sources in high-speed jets via correlation measurements. *J. Fluid Mech.* **537**, 349–385.

PAPAMOSCHOU, D. 2011 Wavepacket modelling of the jet noise source. In *17th AIAA/CEAS Aeroacoustics Conference, Portland, OR, USA*.

PETERSEN, R. A. & SAMET, M. M. 1988 On the preferred mode of jet instability. *J. Fluid Mech.* **194** (1), 153–173.

PICARD, C. & DELVILLE, J. 2000 Pressure velocity coupling in a subsonic round jet. *Intl J. Heat Fluid Flow* **21** (3), 359–364.

SCHAFFAR, M. 1979 Direct measurements of the correlation between axial in-jet velocity fluctuations and far field noise near the axis of a cold jet. *J. Sound Vib.* **64** (1), 73–83.

SCHLICHTING, H. 1979 *Boundary-Layer Theory*. McGraw-Hill.

SUPONITSKY, V., SANDHAM, N. D. & MORFEY, C. L. 2010 Linear and nonlinear mechanisms of sound radiation by instability waves in subsonic jets. *J. Fluid Mech.* **658**, 509–538.

SUZUKI, T. & COLONIUS, T. 2006 Instability waves in a subsonic round jet detected using a near-field phased microphone array. *J. Fluid Mech.* **565**, 197–226.

TAM, C. K. W. & BURTON, D. E. 1984 Sound generated by instability waves of supersonic flows. Part 2. Axisymmetric jets. *J. Fluid Mech.* **138**, 273–295.

TAM, C. K. W. & CHEN, P. 1994 Turbulent mixing noise from supersonic jets. *AIAA J.* **32** (9), 1774–1780.

THOMPSON, K. W. 1987 Time dependent boundary conditions for hyperbolic systems. *J. Comput. Phys.* **68** (1), 1–24.

TINNEY, C. E., GLAUSER, M. N. & UKEILEY, L. S. 2008 Low-dimensional characteristics of a transonic jet. Part 1. Proper orthogonal decomposition. *J. Fluid Mech.* **612**, 107–141.

TINNEY, C. E. & JORDAN, P. 2008 The near pressure field of co-axial subsonic jets. *J. Fluid Mech.* **611**, 175–204.

TOMKINS, C. D. & ADRIAN, R. J. 2005 Energetic spanwise modes in the logarithmic layer of a turbulent boundary layer. *J. Fluid Mech.* **545**, 141–162.

TUTKUN, M., GEORGE, W. K., FOUCAUT, J. M., COUDERT, S., STANISLAS, M. & DELVILLE, J. 2009 In situ calibration of hot wire probes in turbulent flows. *Exp. Fluids* **46** (4), 617–629.

VIOLATO, D. & SCARANO, F. 2011 Three-dimensional evolution of flow structures in transitional circular and chevron jets. *Phys. Fluids* **23** (12), 124104.

YULE, AJ 1978 Large-scale structure in the mixing layer of a round jet. *J. Fluid Mech.* **89** (3), 413–432.